EBIT charge-exchange measurements and astrophysical applications[1]

B.J. Wargelin, P. Beiersdorfer, and G.V. Brown

Abstract: The past decade has seen a surge of interest in astrophysical charge exchange (CX). The impetus was the discovery of X-ray emission from comets in 1996, soon followed by the observation of CX emission in planetary atmospheres and throughout the heliosphere. Geocoronal and heliospheric CX are now recognized as contributing a considerable fraction of the soft X-ray background, and stellar-wind charge exchange is expected to occur in the astrospheres surrounding many stars. CX may also contribute to X-ray line emission in supernova remnants, the Galactic Center, and the Galactic Ridge. This article summarizes the key aspects of CX X-ray emission and its astrophysical relevance, and reviews related laboratory measurements and theoretical predictions with particular attention to spectroscopy experiments conducted on electron beam ion traps.

PACS Nos.: 32.30.Rj, 34.70.+e, 39.10.+j, 95.30.Dr

Résumé : La dernière décennie a vu croître l'intérêt pour les réactions d'échange de charge (CX) en astrophysique. La raison vient de la découverte d'émission-X par les comètes en 1996, rapidement suivie par l'observation d'émission CX dans les atmosphères planétaires et dans toute l'héliosphère. Nous croyons aujourd'hui que ces deux derniers types de source contribuent une fraction importante du signal de fond de rayons-X mous et on peut s'attendre à des échanges de charge dans les vents stellaires que l'on retrouve dans les atmosphères entourant beaucoup d'étoiles. Les émissions CX peuvent contribuer aux émissions-X dans les vestiges de supernova, le centre galactique et la dorsale galactique. Nous présentons ici un sommaire des aspects clés de l'émission-X par mécanisme CX et de son intérêt en astrophysique et passons en revue les mesures en laboratoire et les calculs théoriques pertinents, portant une attention spéciale aux expériences de spectroscopie faites à l'aide de pièges électroniques à faisceau d'électrons.

[Traduit par la Rédaction]

1. Introduction

In addition to electron impact excitation, an atomic process known to every astronomer and physicist, there are other line excitation processes including radiative recombination cascades, inner-shell ionization, and the somewhat exotic duo of dielectronic recombination and resonant excitation. An even more obscure process called charge exchange (CX), also known as charge transfer, is of interest to astrophysicists chiefly for its role in determining the ionization balance in H I regions via reactions such as $O^+ + H \rightarrow O + H^+$ [1, 2], or in partially sweeping neutral H away from the Sun via CX with solar-wind protons, thus creating "pickup ions" and contributing to the formation of a neutral H density enhancement on the leading edge of the heliosphere [3].

In the past decade, however, CX has gained the attention of X-ray astronomers as the emission mechanism in a surprising range of astrophysical sources, and for a variable background present in *all* X-ray observations. In Sect. 2, we review the basic features of charge exchange emission and spectra, followed in Sect. 3 by astrophysical examples. Section 4 discusses experimental methods for studying CX, Sect. 5 presents results from electron beam ion trap (EBIT) experiments and compares them with theoretical predictions, and Sect. 6 concludes with a discussion of key issues to be addressed by future laboratory and observational work.

2. Charge exchange basics

2.1. The mechanism

Charge exchange is the semiresonant transfer of one or more electrons from a neutral atom or molecule to an ion. CX between ions *can* occur, but the cross sections are very small because of Coulombic repulsion. By convention, the ion is referred to as the "projectile" because it is usually moving faster than the neutral "target". During the transfer collision, the energy levels of both the projectile and target are distorted as the electric fields of their nuclei and electron(s) are superposed. At certain internuclear distances, energy levels of the projectile and target overlap at "curve crossings" so that an electron from the neutral target may be radiationlessly transferred to the projectile ion. The cross section for this process is very large compared to that for electron impact excitation, typically of order 10^{-14} cm^2.

Because curve crossings occur at several internuclear distances, electrons can be captured into several different energy

B.J. Wargelin.[2] Harvard-Smithsonian Center for Astrophysics, 60 Garden Street, Cambridge, MA 02138, USA.
P. Beiersdorfer and G.V. Brown. Department of Physics, Lawrence Livermore National Laboratory, Livermore, CA 94550, USA.

[1] Paper given at the Workshop on Twenty Years of Spectroscopy with EBIT held in Berkeley, California, 13–15 November 2006.
[2] Corresponding author (e-mail: bwargelin@cfa.harvard.edu).

levels, imparting a semiresonant character to the CX process. If the recipient ion is highly charged, it is the higher lying energy levels that overlap with the neutral's energy levels. A CX collision then results in the capture of an electron into a high-n level of the ion from which it can radiatively decay, releasing an X-ray photon either at the end of a radiative cascade or by decaying directly to the ground state.

If the neutral species has more than one electron (i.e., is anything other than atomic H), multiple electrons may be transferred, creating a multiply excited ion that can either radiatively stabilize or autoionize. For the ions and collision energies of interest here — those that give rise to X-ray emission — the cross sections for multiple transfer are usually smaller than those for single-electron capture (SEC), and most of our discussion will focus on SEC.

2.2. General equations

It can be shown [4] that for an ion of charge q, the energy level having the maximum probability of being populated in a collision with a H atom can be approximated by

$$n_{\max} \sim q \left(1 + \frac{q-1}{\sqrt{2q}}\right)^{-1/2} \sim q^{3/4} \tag{1}$$

For single-electron capture from species other than H, $n_{\max}$ can be approximated by including an additional factor of $\sqrt{I_H/I_n}$, where I_H and I_n are the ionization potentials of H and the neutral target, respectively.

At relatively low collision energies (below $\sim$100 keV/amu), the n distribution is fairly narrowly peaked about $n_{\max}$. As collision energy increases, the n distribution gradually broadens until a critical energy given by

$$E_{\text{crit}} \sim 25\sqrt{q} \quad \text{keV/amu} \tag{2}$$

is reached. At even higher energies, $n_{\max}$ slowly decreases and the distribution narrows again [5].

As an example, in the collision of O^{8+} and H, the most likely level to be populated in the resultant O^{7+} ion is $n_{\max} \sim 5$. At first glance this may seem rather surprising, since the binding energy of that $n = 5$ electron is 35 eV, much more than the 13.6 eV binding energy of the H atom from which it was captured. This is because the electron sees a higher combined electric field as the two nuclei approach each other; the curve crossing occurs when the total binding energy of the electron is significantly larger than its final binding energy of 35 eV in the isolated O ion. In effect, some of the kinetic energy of the collision is converted into potential energy, the so-called "energy defect." Following the electron capture, the O^{7+} ion is left in an excited state with an energy 836.5 eV above the ground state. Details of the resulting decay, which releases at least one photon (an X-ray), are given in Sect. 5.2.

Cross sections for CX have relatively little dependence on the collision energy or target species. At energies extending from well below 1 keV/amu up to E_{crit}, the cross section can be roughly approximated as

$$\sigma_{\text{CX}} \sim q \times 10^{-15} \quad \text{cm}^2 \tag{3}$$

Fig. 1. Theoretical cross sections for $Fe^{q+} + H$ based on results from ref. 6. Labels on each curve indicate the value of q.
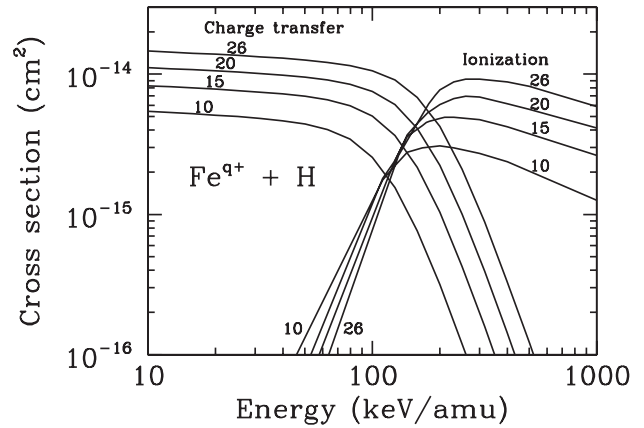
At higher energies, the CX cross section rapidly declines while the cross section for ionization of the projectile (known as "charge stripping") rises and then gradually falls (see Fig. 1).

A more accurate approximation for CX cross sections, based on results from the classical trajectory Monte Carlo (CTMC) modeling method (see, for example, refs. 7 and 8), with uncertainties of $\sim$30% below E_{crit} and roughly 50% at higher energies is provided by Katsonis et al. [6]

$$\tilde{\sigma} = \frac{A \ln (B/\tilde{E})}{1 + C\tilde{E}^2 + D\tilde{E}^{4.5}} \left(10^{-16}\, \text{cm}^2\right) \tag{4}$$

where $\tilde{\sigma} = \sigma_{\text{CX}}/q$, $\tilde{E} = E/q^{0.5}$ (in keV/amu), $A = 0.400\,96$, $B = 2.44 \times 10^6$, $C = 2.5592 \times 10^{-4}$, and $D = 9.049\,85 \times 10^{-8}$. There is no general equation for ionization cross sections below E_{crit}, but σ_{ioniz} peaks around $E = 50/q^{0.415}$ keV and scales at higher energies as q^2/E [6]. At very low energies (up to a few hundred eV/amu) cross sections may deviate significantly from (3) and (4) for some ion/target combinations.

2.3. Collision-energy regimes

Because CX cross sections have a relatively simple form when expressed in terms of $E/q^{0.5}$ and q is roughly one half the number of nucleons for highly charged ions, collision energies are typically expressed in terms of energy per atomic mass unit (for example, eV/amu). The $\sqrt{q}$ dependence also appears in the equation for E_{crit} (2). For ions of interest to X-ray astronomers — mostly bare, H-like, and He-like ions from C to Fe, plus L-shell ions of Fe and some lower Z elements — E_{crit} is roughly 100 keV/amu. Energies below E_{crit} are usually referred to as "low", energies above as "high", and energies within a factor of two or three of E_{crit} as "intermediate". Below roughly 1 eV/amu, collisions are slow enough that electron–electron interactions and pseudo-molecular effects become important, and CX cross sections at these ultra-low energies may differ significantly from those given by (4).

The collision energies relevant to this paper are all above 1 eV/amu. For comparison, typical temperatures of X-ray emitting plasmas range from roughly 10^6 to 10^8 K. From $(1/2)mv^2 = (3/2)kT$, a 10^7 K plasma temperature corresponds to 162 eV/amu for O ions and 46 eV/amu for Fe, with collision energies scaling in proportion to T. Although the fraction of

neutral gas at such temperatures is completely negligible for plasmas in equilibrium, there are instances where astrophysical plasmas may undergo CX with adjoining neutral gas clouds (see Sects. 3.1 and 3.3).

As discussed in Sect. 3.2, the solar wind is responsible for the best known examples of X-ray CX emission and can be divided into two main components: the slow wind, with a typical velocity of 200–600 km/s (0.2–1.9 keV/amu), and the fast wind, with a velocity of 600–800 km/s (1.9–3.3 keV/amu) [9]. Note that the bulk-motion kinetic energy of solar-wind ions is much larger than the thermal energy acquired during their formation in the solar corona, with $T \sim 2 \times 10^6$ K corresponding to ~0.2 keV, or of order 0.01 keV/amu.

Cosmic rays have much higher energies, greater than roughly 1 GeV/amu, and their cross sections for CX are very small (see Fig. 1). There is, of course, a continuum of cosmic-ray energies extending to low energies, but the low-E interstellar flux can not be directly measured because of "solar modulation", in which the solar wind and the magnetic field it carries act to deflect low-energy cosmic rays from penetrating the heliosphere [10]. These particles, with energies from roughly 10 keV/amu to 1 GeV/amu, are sometimes referred to as suprathermal ions. It has been suggested that cosmic rays with energies below ~1 MeV/amu might contribute substantially to X-ray line emission in the Galactic plane but, as discussed in Sect. 3.3, this is unlikely.

2.4. Models and multiple electrons

The preceding discussion and equations have focused on single-electron capture, which produces a singly excited ion that always radiatively decays. Multi-electron capture, of which double-electron capture (DEC) is most common, opens up a much more complicated world of autoexcitation, correlated double capture, true double capture, correlated transfer and excitation, and autotransfer to Rydberg states. Chesnel et al. [11] present an overview of such processes in the context of DEC in Ne^{10+} + He with astrophysically relevant collision energies between 50 eV/amu and 15 keV/amu.

Modeling even SEC involving multi-electron targets is much more difficult than for simple ion/H collisions, and modeling DEC adds another large step of complexity. The most common theoretical technique used in CX modeling is the classical trajectory Monte Carlo (CTMC) method [7, 8], which provides the predictions of level-specific population distributions necessary for spectral modeling, unlike some other methods. Although theoretical calculations for collisions involving fully stripped ions and atomic H are essentially exact because of the simplicity of the system (just two nuclei and one electron), the CTMC method is difficult to extend to other systems and most versions treat multi-electron targets simply as atomic H with a modified ionization potential. Not surprisingly, results from experiments with multi-electron targets often have significant disagreements with CTMC model predictions (see Sect. 5.4). Models also become more complicated as the number of projectile electrons increases, and very little theoretical work has been done on anything other than hydrogenic or fully stripped ions.

A discussion of current approaches to CX modeling is beyond the scope of this paper, but Sect. 4 of the review on cometary CX emission by Krasnopolsky et al. [12] gives an excellent summary of theoretical methods and results. Each method has a limited range of applicability, particularly in terms of collision energy, but the limits are generally not well-known and model uncertainties are difficult to estimate. The problem is even greater when modeling CX spectral emission, which depends very strongly on the initial distribution of angular momentum states following electron transfer (see Sects. 5.2 and 5.3). Experimental results are thus vital in guiding the development of theory, but as seen in the Oak Ridge National Laboratory/University of Georgia Charge Transfer Database for Astrophysics (http://cfadc.phy.ornl.gov/astro/ps/data/), very little experimental data exist for astrophysically relevant CX collisions, even with H as the target. Level-specific data (i.e., cross sections for individual nl levels) and spectra are even scarcer, often making it difficult to interpret astrophysical observations, for which spectra are often the only source of information.

3. Astrophysical relevance

3.1. Photoionized and nonequilibrium plasmas

One area where the significance of CX has been appreciated for some time is in calculations of ionization balance. For collisional plasmas in equilibrium, CX is generally of minor importance, but in photoionized plasmas, in interactions of the interstellar medium (ISM) with stellar winds and cosmic rays, and in nonequilibrium situations such as supernovae and evaporating clouds, CX can have a significant effect on the ionization balance, as well as on the thermal evolution of the system via line emission.

As explained by several authors (see, for example, refs. 13 and 14), CX can be at least as important as radiative recombination (RR) and dielectronic recombination (DR) in photoionized plasmas; the photoionization cross section of atomic hydrogen decreases rapidly with photon energy ($\sigma_{PI} \propto E^{-3.5}$), so highly charged ions can coexist with a non-negligible population of neutral hydrogen and helium atoms. Because cross sections for CX are usually orders of magnitude larger than those for RR and DR, even a tiny fraction of neutral gas can have a large effect on the overall plasma ionization state.

The tabulations of ionization and recombination cross sections used in such calculations [15–17], however, generally apply broad extrapolations of the little data available, and use only *total* CX cross sections. If some emission lines are optically thick (for example, in binary accretion disks), the details of the CX spectrum become important; for example, photons from optically thin high-n transitions in H-like ions (see Sect. 5.2) can escape from and thus cool dense gas much more easily than Lyα photons.

CX may also play an observable role in the ionization (non)-equilibrium of supernova remnants, particularly at the interfaces of hot shocked plasma and relatively cool, dense clouds within the remnant. Wise and Sarazin [18] estimated how much CX X-ray emission would result from a fast supernova remnant shock without such clouds and concluded that no more than about 10% of the emission from He-like carbon and nitrogen would arise from CX, and less from other elements. Lallement [19] likewise calculated that CX emission is minor for a supernova

Table 1. Average abundances of highly charged ions in the solar wind. Element abundances (relative to O) are taken from Steiger et al. [29]. Ion fractions are from Schwadron and Cravens [30].

Ion	Slow wind		Fast wind	
	Element abund.	Ion fraction	Element abund.	Ion fraction
C^{5+}	0.67	0.210	0.69	0.440
C^{6+}	0.67	0.318	0.69	0.085
N^{5+}	0.078	0.065	0.113	0.127
N^{6+}	0.078	0.058	0.113	0.011
N^{7+}	0.078	0.006	0.113	0.000
O^{6+}	1.00	0.730	1.00	0.970
O^{7+}	1.00	0.200	1.00	0.030
O^{8+}	1.00	0.070	1.00	0.000
Ne^{7+}	0.097	0.004	0.083	0.005
Ne^{8+}	0.097	0.084	0.083	0.102
Mg^{9+}	0.145	0.052	0.106	0.044
Mg^{10+}	0.145	0.098	0.106	0.029

blast wave propagating in a partially neutral ISM. Wise and Sarazin suggested, however, that the role of CX would be enhanced by hydrodynamic instabilities, or inhomogeneities in the interstellar gas (particularly long filaments with large surface areas), as may occur in relatively young remnants, and Lallement noted that there are line-of-sight enhancements to CX emission intensity along interfaces between ionized and neutral gas.

Although there has been speculation over possible signatures of X-ray CX in SNRs [20], thus far there is no clear evidence for such emission. This may be in part because X-ray detector efficiency and intrinsic resolving power are typically very low for the lines predicted to be most affected (He-like C and N), making detection of any CX features difficult.

In addition to supernovae, Lallement [19] also considered CX emission from high-velocity clouds moving through the Galactic halo, and dense clouds interacting with galactic winds or intra-cluster gas. Lallement concluded that CX might contribute a significant fraction of the total emission in each case, particularly in individual lines. Detecting that emission will require future large-area X-ray missions using nondispersive imaging detectors with good energy resolution, such as the microcalorimeter [21] used on the Lawrence Livermore EBIT (see Sect. 4.1.1).

3.2. Solar-wind charge exchange
3.2.1. Comets
Renewed interest in astrophysical CX was triggered by the discovery of X-ray emission from comets in a 1996 observation of comet Hyakutake by the ROSAT observatory [22]. Soon afterward, Cravens [23] proposed that highly charged heavy ions in the solar wind undergo CX with neutral gas evaporating from the cometary nucleus (mostly H_2O, CO, and CO_2). Since then, more than 20 comets have been observed to emit X-rays and extreme ultraviolet radiation by missions including ROSAT, EUVE, ASCA, BeppoSAX, Chandra, XMM-Newton, and Swift, and the solar-wind charge exchange (SWCX) explanation is now well-established.

Cravens [24] reviewed cometary X-ray emission in 2002, and a summary of observations up to 2004 is provided by Lisse et al. [25] and Krasnopolsky et al. [12]; the latter also discuss CX modeling and laboratory experiments. The most recent summary of comet observations (covering most of 2006, but not Sasseen et al. [26] or Krasnopolsky [27]) is part of a review by Bhardwaj et al. [28] that covers all sources of X-ray emission throughout the solar system.
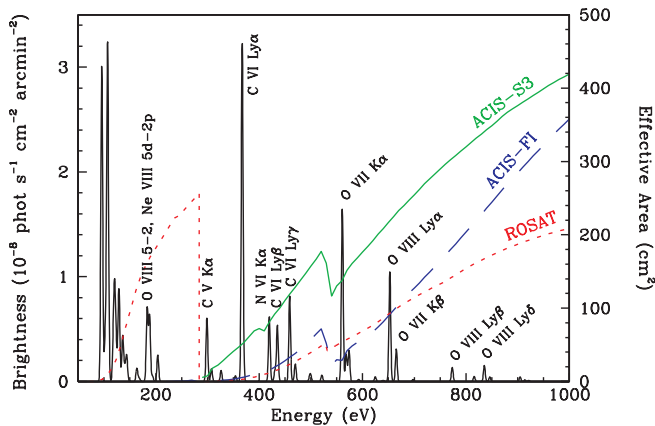
3.2.2. Spectra
X-ray emission from comets was very surprising at first since comets have temperatures of order 100 K while X-ray emission is characteristic of matter at temperatures of millions of degrees. Cravens [23] recognized that the real source of the X-rays is the solar wind; highly charged ions in the wind capture electrons from neutral gas and decay to ground, thus releasing some of the potential energy of their highly charged states that was originally acquired by thermal ionization in the two-million-degree solar corona.

There are two main components of the solar wind: the fast wind, with a typical velocity of 750 km/s, and the slow wind, which is more highly ionized than the fast wind and has an average velocity of 400 km/s [9]. During a solar minimum, when the Sun's corona is at its least active point during the 11 year solar cycle (as it will be during 2007), the slow wind is confined to within about 20° of the ecliptic while the fast wind is found at higher solar latitudes. During a solar maximum the two components are much more mixed, with a predominance of slow wind at most latitudes.

Although neutral target species may vary somewhat from one X-ray source to another (for example, H_2O in comets, H in planetary atmospheres), all SWCX spectra are similar because they share the same source of emission — solar-wind ions. Table 1 lists average abundances of the "metals" in the slow and fast solar wind that are most important to X-ray CX emission [29, 30]. The most abundant metal ions are the bare, H-like, and He-like charge states of C and O; during coronal mass ejections, the fraction of highly charged ions is much larger and

Fig. 2. Model geocoronal CX spectrum (4 eV resolution) for CX between slow solar-wind ions and atomic H, and effective areas for the ROSAT position-sensitive proportional counter, and the Chandra ACIS-S3 and front-illuminated (FI) CCDs. Adapted from ref. 35.

Fig. 3. Spectrum of Comet LINEAR C/1999 S4 observed by Chandra (+), with fit (continuous line) based on laboratory CX spectra obtained by the ASTRO-E microcalorimeter on the LLNL EBIT (colored emission lines). Adapted from ref. 36.

may include bare and H-like Ne and Mg, and enhancements in the population of L-shell Fe ions. Bare ions charge exchange to produce H-like ions and Lyman series emission, H-like ions charge exchange to produce He-like ions and what we will refer to as "K-series" emission, and He-like ions charge exchange to produce Li-like ions and $n \to 2$ emission. (We focus on single-electron capture; multielectron CX is discussed in Sect. 5.4).

A number of theoretical SWCX spectra have been created based on experimental cross sections and calculated radiative rates, for CX between the slow or fast wind and H, He, or cometary neutrals [31–34]. Model spectra for SWCX with H [35] are shown in Fig. 2. Although carbon and oxygen have comparable SWCX X-ray intensities, O emission lines are the most prominent features in observed spectra because C lines are emitted at energies where X-ray detection efficiency is usually low. An observed comet spectrum is shown in Fig. 3 along with a fit based on laboratory CX spectra [36].

3.2.3. Planetary atmospheres

Soon after the discovery of cometary X-rays, the concept of SWCX emission was expanded to include emission from planetary atmospheres and the heliosphere. Chandra and XMM-Newton have each observed Mars [37–39], revealing the presence of a faint halo of CX emission surrounding the planet, in addition to fluorescent emission from the illuminated disk. The source of neutral gas for CX is mostly atomic H in the extended outer atmosphere, or exosphere, extending tens of thousands of kilometres into space. Although faint, XMM-Newton grating spectra clearly reveal CX emission lines of C and O at the expected wavelengths [39].

CX emission has also been observed in Jupiter's aurorae by Chandra [40, 41] and XMM-Newton [42, 43], although it is not clear if the emitting ions are from the solar wind or the Io Plasma Torus [44–46]. In the former case, the CX emission would comprise H-like and He-like C and O lines, while in the latter the emission would be from O and L-shell S. In either case, it appears the ions are accelerated by Jupiter's magnetosphere
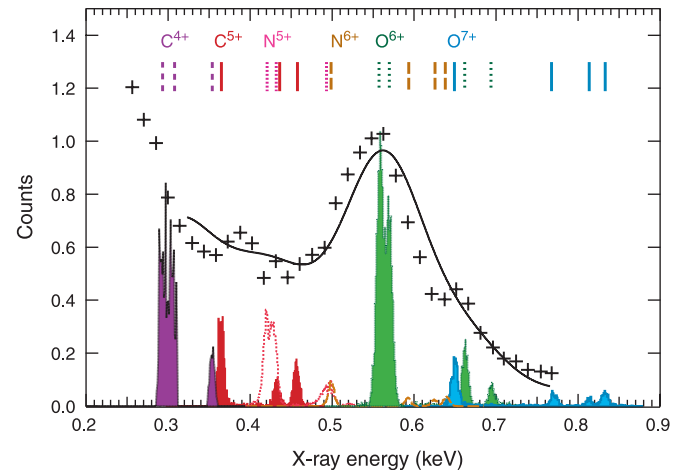
to velocities of at least ∼5000 km/s (∼130 keV/amu) [43]. Particle measurements at Jupiter by the New Horizons mission in February–March 2007 as it receives a gravity boost on its way to Pluto, in coordination with observations by Chandra, XMM-Newton, Hubble, and other ground- and space-based telescopes, should help resolve many questions regarding Jupiter's auroral emission.

Venus has been observed multiple times by Chandra and although its exospheric CX emission is expected to be stronger than that of Mars because of its larger size and the higher density of the solar wind, no CX signal has yet been detected. The first observation occurred in early 2001 near solar maximum when solar X-ray emission is at its brightest, and fluorescent emission (O–K from atmospheric CO_2) presumably obscured the predicted CX signal [47]. Results from subsequent observations conducted in March 2006, near solar minimum, have not yet been published but are expected to reveal CX emission from O and perhaps C and Ne. Another Chandra observation is scheduled for October 2007 in concert with in situ measurements of the solar wind by Venus Express.

3.2.4. Earth and geocoronal CX

CX emission from the Earth's exosphere has also been observed. This geocoronal emission is present in the backgrounds of all Earth-orbiting X-ray satellites, but its presence is usually hard to discern. Indications of its existence came during the ROSAT mission, which conducted an all-sky survey between 100 eV and 2.5 keV (usually broken into 1/4, 3/4, and 1.5 keV bands). Long-term enhancements (LTEs) in the observed soft X-ray emission were occasionally observed [48], and it was later noted that these enhancements sometimes seemed to be correlated with solar-wind variations [49].

The temporal connection between the solar-wind variations, SWCX, and LTEs was proven a decade after the ROSAT survey by Cravens et al. [50], and spectral confirmation was provided by a series of Chandra observations of the Moon [35]. With the Moon blocking out the cosmic X-ray background, the fore-

Fig. 4. Top panels: Background-subtracted spectra from Chandra observations of the dark Moon [84], showing geocoronal CX emission lines (see Fig. 2). O Kα and Lyα are nearly resolved in the FI spectrum, which has better resolution than the S3 spectrum. Bottom panels: Model CX spectra convolved with detector responses; S3 has higher efficiency at low energies than the FI CCDs. The dotted blue curves are for the average slow solar wind (as in Fig. 2). The continuous red curves have been adjusted to better match the observed spectra by lowering the carbon and H-like O abundances. Mg is not included in the model, but He-like Mg Kα appears with 3σ significance in the FI spectrum at 1354 eV. Note that S3 and FI data were not collected entirely simultaneously.
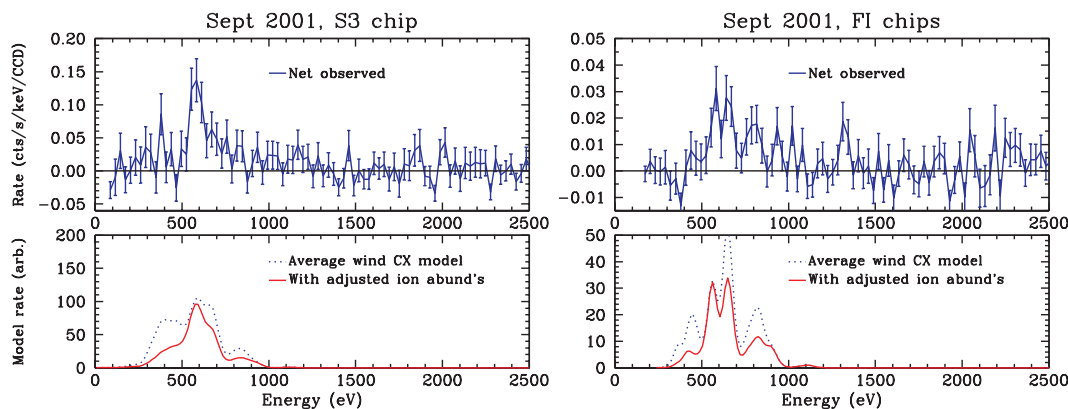
ground geocoronal CX emission was revealed (see Fig. 4) with an intensity that approximately matched model predictions incorporating measured values of solar-wind density, velocity, element abundances, and ionization state. Since then, LTE-like variations in the soft X-ray background have been noted in several observations by missions including Chandra [51, 52], XMM-Newton [53 and Fig. 49 of 28], and Suzaku [54, 55]. An example is shown in Fig. 5 comparing several Suzaku observations of the ecliptic pole [54].

As discussed in papers modeling the interaction of the solar wind with the Earth's magnetosphere [56–58], geocoronal emission is strongest in the Sunward direction where the solar wind compresses the magnetosphere, allowing solar-wind ions to charge exchange in relatively dense regions of the outer atmosphere. In the downwind direction, geocoronal emission is negligible because the solar wind is excluded from the magnetotail. The SWCX emission observed by X-ray satellites depends not only on where they are looking, but also where they are looking from, which may be well above or within regions of high CX emissivity.

3.2.5. The heliosphere

Although the density of neutral gas in the heliosphere is much less than in the geocorona (roughly 0.1 cm^{-3} versus of order 10 cm^{-3}), the volume and total amount of gas is much larger. Soon after cometary X-ray emission was recognized to be the result of SWCX, Cox [59] suggested that a diffuse glow of CX emission might permeate the entire heliosphere as neutral H and He from the interstellar medium flowed into the solar system and interacted with the solar wind. Cravens [60] studied this idea quantitatively and concluded that heliospheric CX emission (as viewed from Earth) was roughly ten times as strong as geocoronal X-ray emission and might account for up to half of the soft X-ray background. Subsequent theoretical work [34, 35, 50, 56, 58, 61, 62] has investigated how heliospheric X-ray emission intensity varies with observer location,

Fig. 5. Suzaku observations comparing a baseline "stable" spectrum (continuous thin line) and a spectrum with enhanced emission (error bars) attributed to a transient increase in the geocoronal CX X-ray background [54]. The enhancement was fitted (continuous thick) with nine lines (dotted) at energies expected for CX emission.
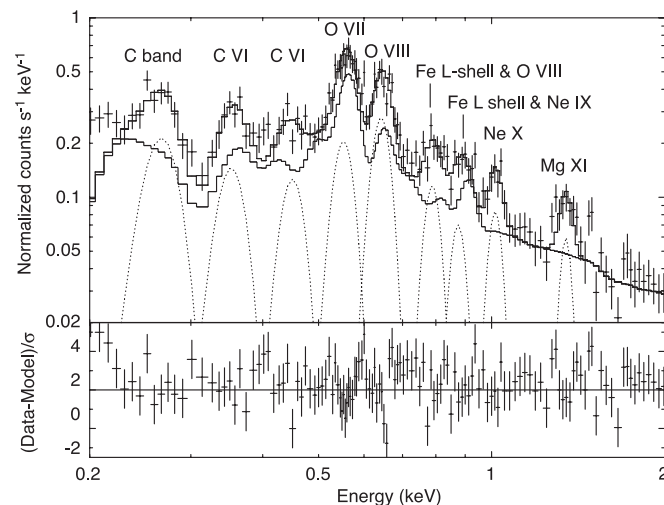
look direction, the solar cycle, and temporal variations in the solar wind. Estimates of the SWCX contribution to the soft X-ray background range from as little as 5–10% in some directions to nearly all the background in some energy bands, although model uncertainties are large. Observations of stellar wind CX have also been proposed to image astrospheres and measure mass-loss rates around nearby late-type stars [63] but existing X-ray observatories do not have quite enough sensitivity [64].

Observational progress on geocoronal and heliospheric CX [35, 51, 53–55, 65, 66] has been slower than for theoretical work given the difficulty of distinguishing CX emission from the true cosmic X-ray background and the weakness of the CX signal,

which is typically of the same order as detector background. Microcalorimeter X-ray detectors, which have much better energy resolution ($\lesssim$ 6 eV FWHM) than the CCDs on Suzaku, XMM-Newton, and Chandra (roughly 50–100 eV FWHM below 1 keV), hold great promise for studies of astrophysical CX, as they can easily discern spectral features that uniquely identify CX emission (see Sects. 5.2 and 5.3). In addition to its potential as a means of studying the Earth's magnetosphere, the heliosphere, and stellar winds and astrospheres around other stars, the existence of SWCX impacts many other astrophysical studies. Our understanding of the local interstellar medium is obviously affected; the temperature and pressure of the Local Bubble are likely lower than has been previously assumed [61], and SWCX may explain the mismatch between Local Bubble emission measures, metal depletions, and H column densities derived from extreme ultraviolet versus X-ray observations [65, 66]. Uncertainty in the SWCX level also affects spectral analyses of extended objects such as supernova remnants and galaxy clusters (for example, apparently red-shifted O VII Kα cluster emission can be explained by local SWCX emission [67, 68]), and is the limiting factor in efforts to detect emission from the Warm-Hot Intergalactic Medium.

3.3. Galactic center and galactic ridge

While SWCX is now well-established, the origin of the Galactic Ridge X-ray Emission (GRXE) remains controversial a quarter century after its discovery [69]. The Galactic Ridge lies within a few degrees of the Galactic Plane and within roughly 45° of the Galactic Center (GC), which it includes. It features apparently diffuse X-ray emission with a spectrum that is virtually the same all along the Ridge, apart from intensity. In addition to strong continuum radiation there are prominent He-like and H-like emission lines from Mg, Si, S, Ar, Ca, and Fe [70–73]. Several explanations for the line emission have been proposed [73, 74 and references therein], including the idea that it arises from the CX of low-energy cosmic rays with neutral gas in the Galactic Plane [75, 76]. An earlier version of this idea was first suggested by Silk and Steigman [77] but subsequent theoretical studies [78–80] concluded that the fraction of nearly fully ionized cosmic rays needed to produce the observed H-like and He-like line emission was negligible below a few MeV/amu (well above E_{crit}), and the cross sections for CX at higher energies were much too small to explain the observed GRXE intensities.

The most recent and likely explanation is a revival of an earlier idea. Based on extrapolations of Rossi-XTE data and noting the close similarity between the GRXE and infrared background emission distributions, Revnivtsev et al. [74] propose that the GRXE arises from the superposition of unresolved coronally active binaries and cataclysmic variables. Other authors [72, 73], however, argue that the required sources would have been resolved in existing Chandra observations of the Galactic Center and that the GRXE is truly diffuse. Spectral comparisons of the GRXE with Fe line diffuse emission from the center of the nearby starburst galaxy M32 are inconclusive [81].

Although the cosmic-ray CX hypothesis looks unlikely, it might be revived if some mechanism is found to extend the range of nearly fully stripped cosmic rays to energies below

1 MeV/amu. (Recall from Sect. 2.3 that no unbiased measurements of interstellar cosmic rays exist below about 1 GeV/amu.) Possibilities may include larger than assumed rates of multielectron ionization of cosmic rays in sub-MeV/amu collisions [80] (for which there are very little experimental data) or reionization of cosmic rays by Galactic magnetic field reconnection [82]. The theoretical studies from the 1970s [78–80] also overlooked increased metal abundances closer to the GC.

The Galactic Center is the brightest part of the Galactic Ridge, with intense thermal emission from abundant hot gas. There are also a number of warm dense molecular clouds, so CX emission from the thermal highly charged ions must be present at some level. However, diffuse thermal emission together with radiation from the dense population of point sources in the GC is very likely to obscure any signature of CX emission, whether from cosmic rays or the interfaces of hot gas and warm clouds. This is confirmed in recent observations of the Galactic Center region by Suzaku that indicate the centroid of the He-like Fe Kα complex has an energy too high to be explained by CX alone [83, 84] (see Sect. 5.3).
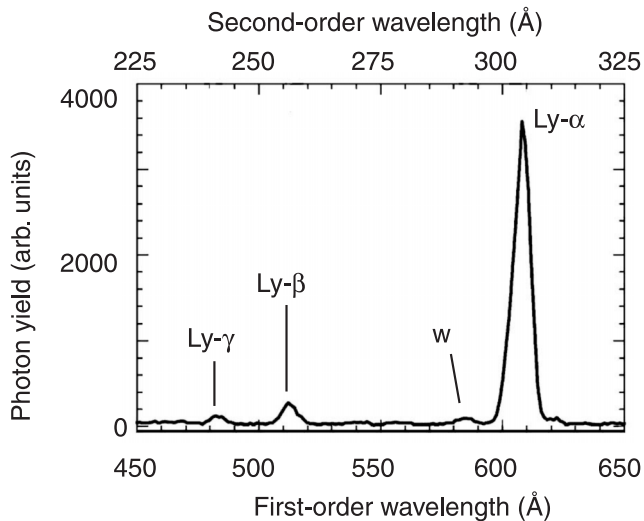
Although more in the realm of gamma-rays than X-rays, solid evidence for the operation of CX in the GC comes from the measurement of the 511 keV annihilation line by INTEGRAL. Based on the line width and shape, Churazov et al. [85] and Jean et al. [86] estimate that nearly all of the observed emission comes from the annihilation of positronium (as opposed to direct e^+ and e^- collisions) and that roughly half of the positronium is formed via the CX of positrons with neutral gas. The positron and electron eventually annihilate, releasing either two 511 keV photons if the e^+ and e^- have opposite spins, or three lower energy photons with a continuum of energies if the spins are the same.

4. Experimental methods

Until the development of electron beam ion traps (EBITs), virtually all measurements of charge exchange involved crossed-beam experiments in which a beam of highly charged ions passes through a source of neutral gas, usually a supersonic gas jet (or "gas cell") inside a chamber with differential pumping. Ion beams can be generated by foil stripping and then injected into a storage ring and held at a constant (very high, MeV/amu) energy (see, for example, ref. 87). As they circle the ring, the ions repeatedly enter a gas cell where they can undergo CX. Electron cyclotron resonance (ECR) sources and electron beam ion sources (EBISs) are also used to provide ions in crossed-beam experiments, typically at energies of a few or tens of keV/amu. Measurements in crossed-beam experiments usually focus on determinations of ion charge, which yield CX cross sections. Studies of photon emission are rare, but are becoming more common.

Some of the first charge-exchange-induced emission spectra of K-shell ions were obtained in a crossed-beam experiment by Greenwood et al. [88, 89]. They studied bare Ne^{10+} and several other lower q ions from an ECR source at the Jet Propulsion Laboratory interacting with H_2O, He, H_2, and CO_2. The data were obtained at ion-neutral collision energies of $\sim$3 keV/amu, comparable to ion energies in the fast solar wind. Similar mea-

Fig. 6. Spectrum of the Lyman series of He^+ formed by CX of He^{2+} with H_2O measured in second order of reflection. Also seen is the $1s2p\ ^1P_1 \rightarrow 1s^2\ ^1S_0$ emission line (w) in neutral helium. The latter transition is observed in first order and is attributed to double-electron capture during CX. The spectrum was obtained at the Kernfysisch Versneller Instituut in Groningen [96, 97] at a collision energy of 48 keV.

Fig. 7. EUV spectrum of N^{4+} formed by charge exchange of N^{5+} with H_2. The spectra were recorded using the crossed-beam facility in Groningen and are recorded in ref. 101 at collision energies of (*a*) 16.5 keV and (*b*) 0.5 keV.

surements conducted with the ECR source at the University of Nevada, Reno, demonstrated the role of multiple electron capture in X-ray line formation by CX [90]. One complication common to all merged or crossed-beam experiments is that ions in metastable states (such as the $1s2s\ ^1S_3$ state in He-like ions) may move well beyond the interaction region before they radiatively decay, making spectral measurements incomplete or harder to interpret. Nevertheless, the combination of charge-state determinations and spectral measurements is a very powerful one, potentially revealing state-specific absolute cross sections for both single- and multi-electron CX. Some relatively recent enhancements of the cross-beam technique provide additional information, particularly state-selective cross sections (i.e., cross sections for individual n and sometimes l levels) by measuring scattering angles and (or) ion kinetic energy losses ("Q values"; for example, refs. 11, 91–95).

One example of a K-shell ion that has been studied using the crossed-beam method is He^{2+}. The ionization potential of hydrogenic He^{1+} is 54.4 eV (corresponding to $\lambda = 228$ Å), so CX reactions involving bare helium form lines in the extreme ultraviolet. A spectrum from CX with H_2O is shown in Fig. 6. The measurement was carried out using 50 keV He^{2+} ions at the Kernfysisch Versneller Instituut in Groningen [96, 97]. While most of the emission is the result of single-electron capture, a small feature corresponding to the $1s2p\ ^1P_1 \rightarrow 1s^2\ ^1S_0$ transition in neutral He is seen. This feature is produced only by "true" double-electron capture, where "true" means that both of the transferred electrons radiatively stabilize, as opposed to one of them being lost by autoionization. As shown by Lubinski et al. [98], the cross section for single capture producing the Lyα line at 304 Å drops as the collision energy decreases, while that for producing the neutral helium line, labeled w at 584 Å in Fig. 6, increases. As a result, the ratio of the Lyα line in He^+ to
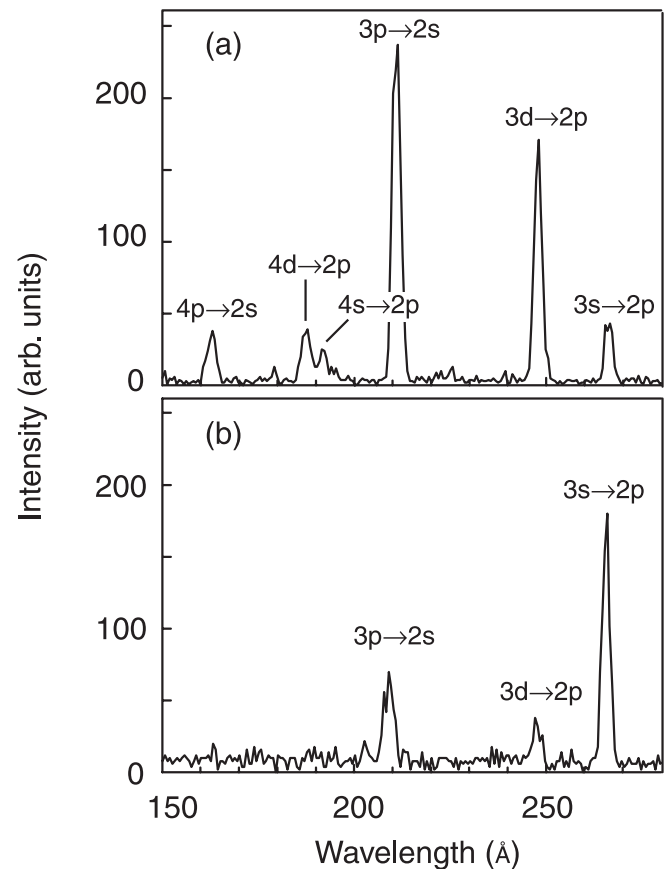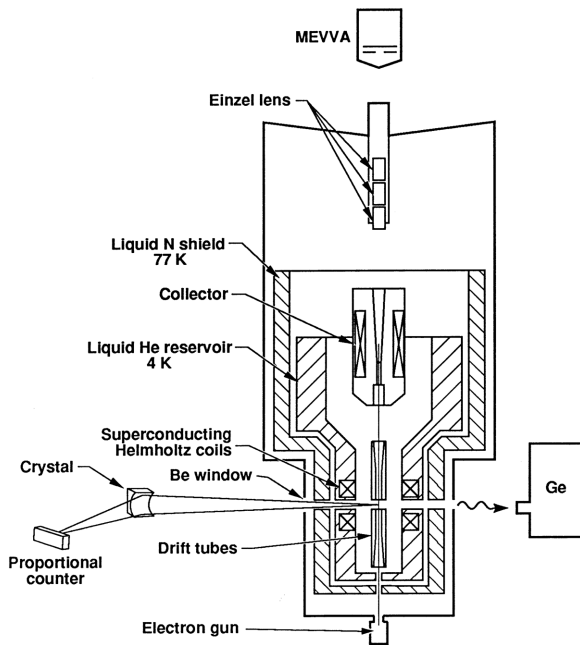
that of w in neutral helium is dependent on the collision energy and can be used to determine the velocity of alpha particles in the solar wind interacting with cometary neutrals [99].

Crossed-beam experiments have also been used to determine CX cross sections and spectral emission from L-shell ions. Such measurements have concentrated on relatively simple L-shell ions, for example, Li-like or Be-like ions [100–102], which are close analogs of H-like and He-like ions, respectively. However, additional lines appear in these spectra because of the fact that the $n = 2$ ground configuration may assume both an $\ell = 0$ and 1 angular momentum state. This is illustrated in Fig. 7, which shows the L-shell emission of Li-like N^{4+} formed in the interaction of N^{5+} with H_2 using the crossed-beam facility at Groningen [101]. Note that the shape of the L-shell emission depends on the collision energy, similar to the behavior of H-like spectra (see Sect. 5.2).

Something like the inverse of the crossed-beam setup takes place in tokamaks, where a neutral beam (usually of H isotopes) is injected into the tokamak's plasma. Trace concentrations of highly ionized elements, either deliberately introduced or present as background impurities, then charge exchange with the neutrals in the beam. The collision energy is largely determined by the neutral-target energy, typically tens of keV/amu, while the thermalized ions have energies of order 100 eV/amu. Using this approach, a spectrum of He-like Ar^{16+} formed by CX

Fig. 8. Schematic cross section of the Livermore electron beam ion trap. Highly charged ions are created by electron collisions and confined in the trap region. Various X-ray detectors ring the trap region to observe the emitted photons.

Fig. 9. Electron beam ion trap drift tube assembly, showing the three drift tubes and the central trap region. The axial potential well is generated by raising the voltage of the two end drift tubes above that of the middle. Ions are radially confined by the electrostatic attraction of the electron beam, which also collisionally ionizes the ions. In the magnetic trapping mode the electron beam is off and radially confinement is provided by the 3 T magnetic field.

of thermal Ar^{17+} ions with an 80 keV beam of neutral deuterium was recorded on the National Spherical Tokamak Experiment (NSTX) at Princeton [103].

In tokamaks, there is a continuous influx of neutral H gas into the plasma because of hydrogen recycling at the wall and the plasma limiters. Deep inside the plasma, little neutral hydrogen exists and the signal produced by CX competes with electron-impact excitation so that the contribution from CX is nearly impossible to isolate. However, tokamaks exhibit a low level of emission arising from CX with trace amounts of neutral H gas near the plasma boundary. In fact, X-ray emission produced by CX near the plasma edge has been observed even from highly charged ions [104, 105] as ion transport diffuses highly charged ions to the edge region where they can interact with neutral hydrogen.

4.1. Electron beam ion traps

This review focuses on CX results from EBITs, which differ from crossed-beam experiments in that the emitting ions are more or less stationary so that complete spectra can be obtained, even from long-lived metastable states. Unlike merged beams, however, EBITs cannot provide absolute cross sections because necessary experimental parameters such as neutral gas density can not be determined with enough precision.

The design and operation of EBITs is described in this volume [106] and elsewhere [107, 108]. EBITs are based on electron beam ion sources but modified specifically for spectroscopic studies of the interaction of highly charged ions with an electron beam. The electrons pass through a 2 cm long trap region and are focused by a $\sim$3 T magnetic field into a beam about 60 μm in diameter (see Figs. 8 and 9). Neutral atoms or ions with low charge from a vacuum arc source are injected into the trap

where they are collisionally ionized and excited by the electron beam, which can be tuned to energies between a few hundred eV and tens or even hundreds of keV. Very high-charge states can be attained, with longitudinal electrostatic confinement of the ions provided by a set of drift tubes. Radial confinement is provided by electrostatic attraction of the electron beam, as well as by the magnetic field. Several slots cut into the drift tubes are aligned with vacuum ports, providing access for spectrometers and other instrumentation.

CX is both a blessing and a curse in EBITs. Early experiments on the original LLNL EBIT were unable to reach the ion charge states expected for a given electron beam energy because the most highly charged ions acquired so much kinetic energy in collisions with electrons that they escaped from the trap. It was noticed that X-ray emission rates, indicative of the number of trapped high-charge ions, would increase momentarily after occasional high-voltage breakdowns, which suggested that a lower quality vacuum caused by the release of contaminants on internal surfaces during the electrical shorts somehow improved trap performance [3]

The solution was to intentionally inject a neutral low-Z gas (usually N_2, although neutral Ti evaporated from a hot wire was also used early on), providing light ions that collided with the heavier ions of interest and carried away excess kinetic energy by escaping from the trap in a process called evaporative cooling [109–111]. Because the energy required for escape is proportional to qV_{trap}, lower Z, lower q coolant ions escape first and allow higher charge states to be attained for the ions of interest. In competition with this process is CX between

---

[3]R.E. Marrs. Private communication. 2006.

neutral gas, either ambient or deliberately injected, and the ions under study. Too much neutral gas suppresses the overall charge balance, and even tiny leaks in EBIT internals can substantially degrade performance.

The collision energy in a CX reaction is given by the energy of the ion, as the energy of the neutral is negligible by comparison. Ion energies are primarily determined by ion charge and trap depth, i.e., by the fact that ions with energy higher than qV_{trap} leave the trap. Ion temperatures have been determined for several combinations of ion charge and trap depth by measuring Doppler-broadened widths of selected X-ray lines with very high-resolution crystal spectrometers [112–115]. Trapped ions were found to have energies below the the qV_{trap} limit, which is not surprising because they interact with lower Z ions used for evaporative cooling. Most experiments run with characteristic ion energies between 1 and 20 eV/amu.

4.1.1. Magnetic trapping mode

In normal operation, with the electron beam turned on, i.e., in the "electron trapping mode", electron–ion collisions ionize and excite the trapped ions. In "magnetic trapping mode" [116] the electron beam is turned off. Longitudinal trapping by the potential well is unaffected and the ions remain confined in the radial direction, although more loosely, by the strong magnetic field.

The main applications of the magnetic trapping mode have been in measurements of radiative lifetimes and CX [117]. In both cases, the emission lines of interest are revealed once emission from electron impact excitation (also known as direct excitation, or DE) ceases. To illustrate the difference in DE and CX emission rates, consider Lyα emission from direct excitation of H-like Ne^{9+} and from CX of fully stripped Ne^{10+} with atomic H. The emission rate for DE (in counts/s) is
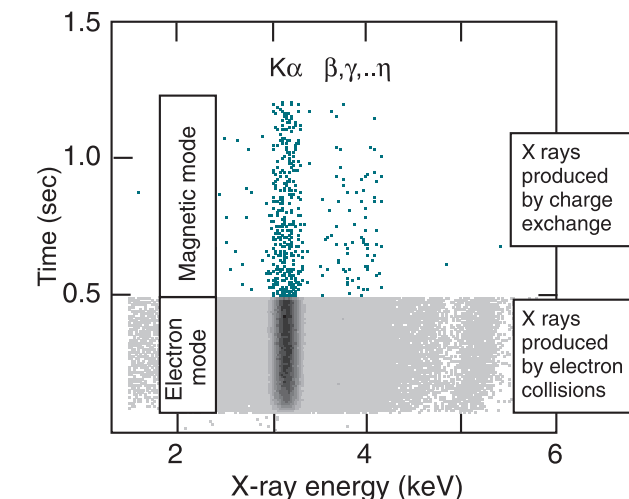
$$R_{DE} = N_i n_e \sigma_{DE} v_e \tag{5}$$

where N_i is the number of emitting ions, n_e is the electron density, σ_{DE} is the cross section for direct excitation of Lyα, and v_e is the electron velocity (effectively the collision velocity because ion velocity is much smaller). The corresponding equation for CX (using the approximation that every CX reaction produces a Lyα photon) is

$$R_{CX} = N_i n_n \sigma_{CX} v_i \tag{6}$$

where n_n is the density of neutral gas, σ_{CX} is the CX cross section for Ne^{10+}, and v_i is ion velocity (effectively the collision velocity because the neutral gas velocity is much smaller).

In both cases the number of emitting ions, N_i, is roughly the same; when the electron beam is on the ions are concentrated around the electron beam, which defines the emitting volume, and when the beam is off the ions expand into a larger cloud, but the composition and total number of ions remains the same [118, 119] and all of them can undergo CX with the neutral gas. There are large differences, however, in n_e and n_n (roughly 10^{12} versus 10^6 cm^{-3}), σ_{DE} and σ_{CX} (10^{-20} versus 10^{-14} cm^2), and v_e and v_i (10^{10} versus 10^6 cm/s), yielding a net DE rate typically several thousand times higher than the rate for CX. When conducting CX experiments, the desired charge state

Fig. 10. Time-resolved spectra of Ar obtained during the electron mode (beam on) and magnetic mode (beam off) phases [120]. The desired charge balance (mostly He-like Ar^{16+} with some H-like Ar^{17+}) is established with the beam on. Charge exchange occurs during both phases but can only be seen when the beam is turned off, revealing He-like Ar K-series emission (Kα, Kβ, ...) from charge exchange between Ar^{17+} and neutral Ar. He-like Ar^{16+} ions also undergo charge exchange, but the resulting Li-like emission occurs below 1 keV.
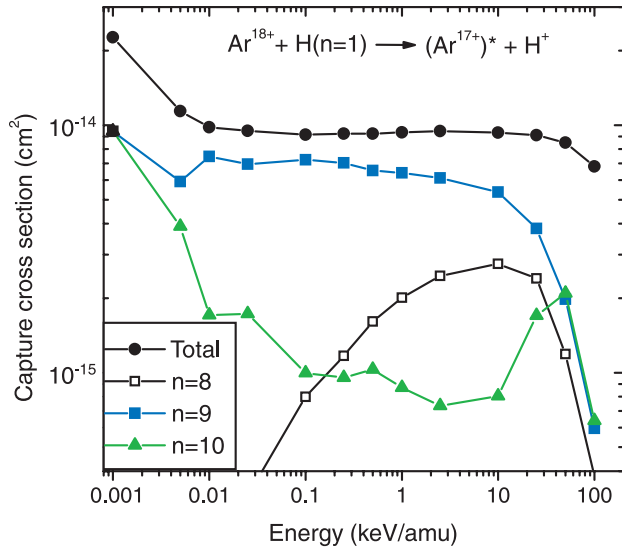

balance is established during the electron-beam-on phase (electron mode) and then the beam is turned off (magnetic mode) to collect the CX spectrum. Example time-resolved spectra are shown in Fig. 10 [120].

When the electron beam is on, electron–ion collisions are essentially unidirectional and the ions' emission is generally polarized. During the magnetic-mode phase, however, ions and neutral gas atoms or molecules collide in random directions and the emission is unpolarized. Although the effects of polarization are routinely taken into account during data analysis, their absence in CX measurements makes analysis easier. The absence of systematic errors introduced by polarization corrections is also beneficial because CX rates are low and statistical uncertainties are relatively large compared to those in DE measurements.

Another difference from DE experiments is that dispersive spectrometers are of little use in collecting CX spectra. The reason is that CX emission arises throughout the relatively large ion cloud in the trap, several hundred μm in diameter. Such a wide source can not be used with grating and Bragg-crystal spectrometers, which rely on the narrowness of the electron beam (60 μm) in lieu of a slit. The CX emission region is so wide that the effective spectrometer resolution is severely degraded, and the use of a slit would block too large a fraction of emission from entering the spectrometer. Nondispersive detectors, such as Ge or Si(Li) solid-state detectors with resolutions of order 100 eV FWHM at 1 keV, are thus essential for CX measurements.

The recent development of X-ray microcalorimeters [121–123] for use in space missions and the laboratory has proven to be a great help to CX studies, as their superior energy res-

Fig. 11. Classical trajectory Monte Carlo model predictions for $Ar^{18+} + H$, showing cross sections for the most important n levels. Adapted from Perez et al. [125].

Fig. 12. CTMC model predictions for the l distribution (of the $n = n_{max} = 6$ level) resulting from charge exchange of Ne^{10+} and H. Adapted from ref. 125.

olution (a few to several eV) allows individual emission lines to be resolved, which is particularly important in disentangling the closely spaced high-n emission lines that are a prominent feature in many CX spectra (see Sect. 5.2). The Lawrence Livermore EBIT group is fortunate to have a collaboration with the Goddard Space Flight Center's X-Ray Spectrometer (XRS) group, who have provided a 6×6-element array microcalorimeter with 32 active pixels for dedicated use on the LLNL EBITs [21]. The XRS is described elsewhere in this volume by Porter et al. [124].

5. Results from experiment and theory

5.1. n and l distributions

As seen in Fig. 1, CX cross sections are roughly constant over a wide range of energy. As discussed in Sect. 2.2, the principal quantum number with the highest likelihood of being populated by electron capture, n_{max}, also has little energy dependence. Theoretical results for the dominant levels populated by the CX of bare Ar^{18+} and H are shown in Fig. 11 [125]. As can be seen, the $n = 9$ level dominates until energies near E_{crit} ($\sim$100 keV/amu).

In contrast to the behavior of the total cross section and n_{max}, the angular momentum distribution has a strong dependence on energy, as seen in Fig. 12 for the $n = n_{max} = 6$ level of H-like Ne following CX between Ne^{10+} and H [125]. At energies below roughly 100 eV/amu, the l-distribution peaks around $l = 1$ while at energies above $\sim$1 keV/amu the l distribution is nearly statistical with $2l + 1$ weightings out to the maximum l value of $l_{max} = n - 1$.

5.2. H-like spectra

Even more than the n-distribution, the l-distribution following electron capture is what determines the form of the emitted spectrum. This is especially true for H-like spectra resulting from CX between a fully stripped ion and a neutral target. At
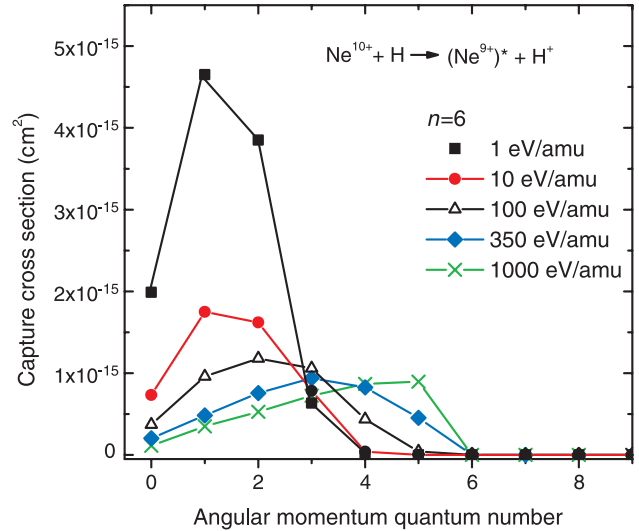
low energies, the captured high-n electron is likely to be in a p state, from which it can decay directly to the 1s ground state yielding a Lyman photon (see Fig. 13; the level for electron capture is $n = 4$ in this example).

At higher energies, higher angular momentum states are preferentially populated, but because of the $\Delta l = \pm 1$ selection rule for electric dipole (E1) radiation, those states can not decay directly to ground. Instead, the high-n electron tends to decay to the lowest n level permitted by selection rules (see Fig. 14). In most cases, especially if the initial n level is large, the first decay will be to an l state where $l = l_{max} = n - 1$, i.e., the maximum angular momentum state for the given n level. From there the electron will decay in $\Delta n = \Delta l = -1$ steps in a "yrast cascade",[4] ultimately releasing a Lyα photon. Only the small fraction of electrons initially captured into p states (along with some electrons that decay to intermediate-n p states) decays directly to ground, so the fraction of high-n Lyman lines is very small.

Examples of EBIT spectra are shown for H-like N ($N^{7+} + CO_2$; [126]) and Ar ($Ar^{18+} + Ar$; [127]) in Figs. 15 and 16. Note the large intensities of the high-n Lyman lines relative to Lyα, especially in the H-like Fe spectrum [84] of Fig. 17, which shows a DE spectrum for comparison. This strong enhancement of high-n Lyman emission is a key feature of low-collision-energy CX spectra. H-like CX spectra have also been obtained using EBITs for $Xe^{54+} + Xe$ [116, 125], $Ne^{10+} + Ne$ [128, 129], and $O^{8+} +$ various molecules [36]; the last two measurements used the XRS microcalorimeter.

The energy dependence of H-like CX spectra is illustrated in Fig. 18 with theoretical results for $O^{8+} + H$ collisions at energies between 1 eV/amu and 100 keV/amu [130]. As can be seen, the

---

[4]Yrast is the superlative of the Swedish word, yr, and means "whirlingest", or "dizziest". In atomic and nuclear physics it refers to the highest angular momentum state for a given principle quantum number. An example of a yrast cascade is
$$5g \rightarrow 4f \rightarrow 3d \rightarrow 2p \rightarrow 1s.$$

Fig. 13. Schematic energy level diagram for a hydrogenic ion illustrating radiative decay paths following charge exchange by a bare ion at low energies. Immediately following electron capture, the resulting H-like ion has a large fraction of states with $l = 1$ (p states) that can decay directly to ground, producing strongly enhanced high-n Lyman emission.
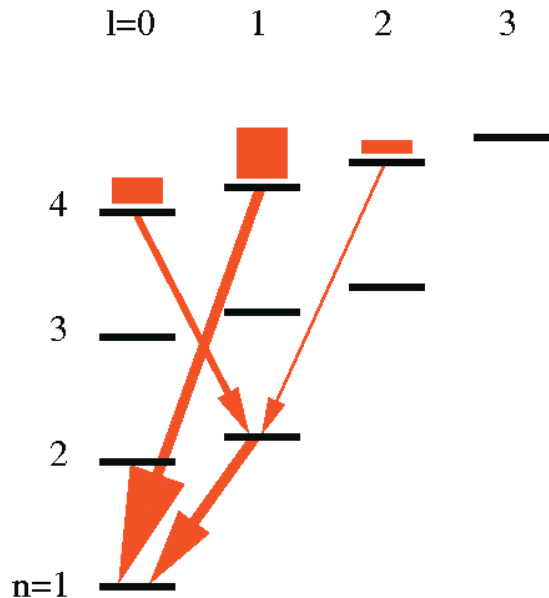

Fig. 14. Radiative decay paths following charge exchange by a bare ion at high energies. The initial l distribution is proportional to $2l + 1$ and most electrons decay to intermediate states with $l = l_{max}$ that then cascade to ground, ultimately releasing a Lyα photon.
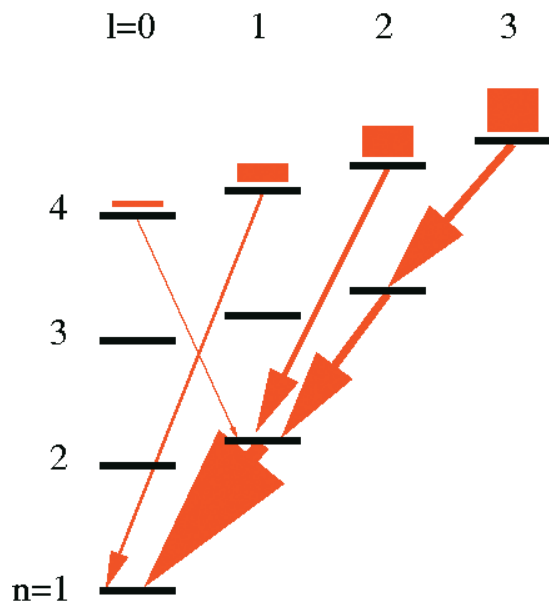

fraction of high-n emission decreases at higher energies, and high-n emission is negligible above a few keV/amu (with a faster fall-off for higher Z elements [125]). The hardness ratio $\mathcal{H} = (\text{Ly}\beta + \text{Ly}\gamma + \text{Ly}\delta + \text{Ly}\epsilon + ...)/\text{Ly}\alpha$ can therefore be used as a collision energy diagnostic.

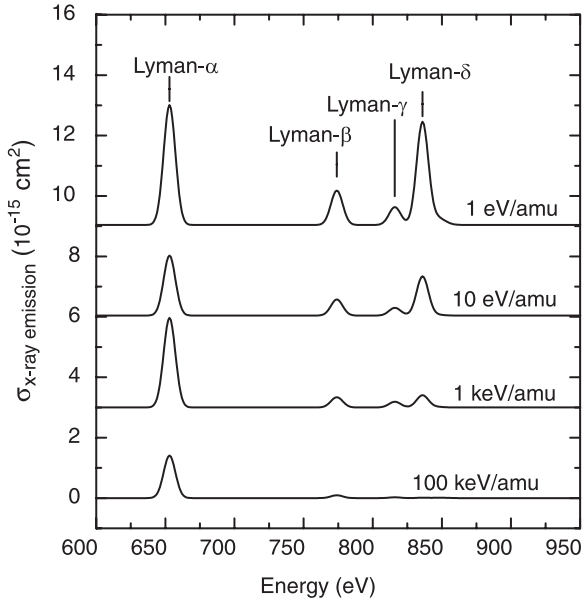**Fig. 15.** H-like spectrum of $N^{7+} + CO_2$ (adapted from ref. 126), obtained using the X-ray spectrometer.
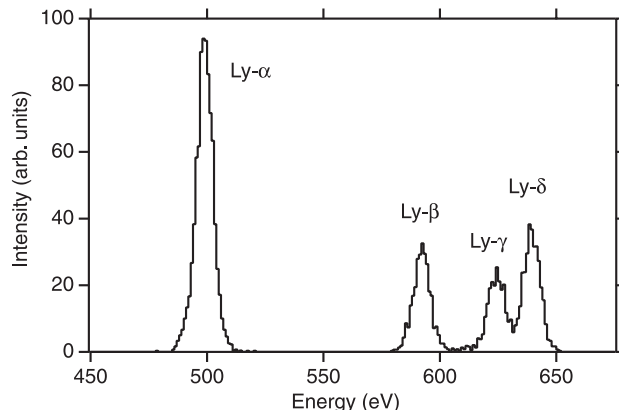
Fig. 16. H-like spectrum of $Ar^{18+} + Ar$. Adapted from ref. 127.
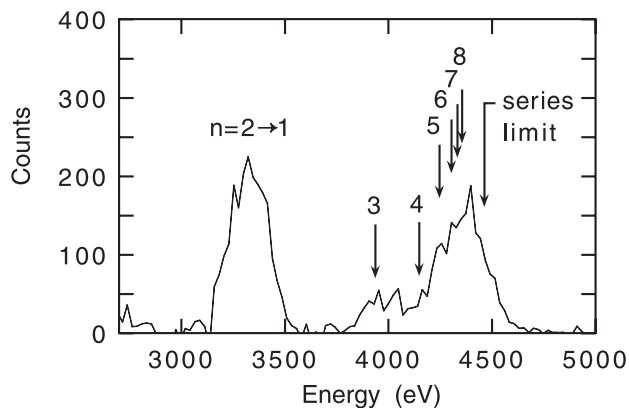
Fig. 17. Electron beam ion trap H-like Fe spectra from direct excitation (top panel) and charge exchange of $Fe^{26+} + N_2$ (bottom; adapted from ref. 84). High-n Lyman emission is strongly enhanced in charge exchange spectra at low collision energies.
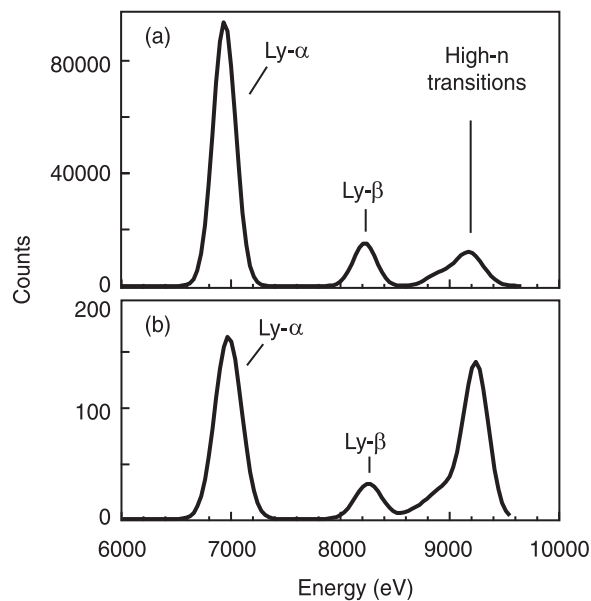
Fig. 18. Classical trajectory Monte Carlo model spectra from charge exchange of O^{8+} and H at energies from 1 eV/amu to 100 keV/amu (adapted from Otranto et al. ref. 130). High-n emission is strongly enhanced at low energies but nearly vanishes as the collision energy approaches E_{crit}.

Fig. 19. Energy level diagrams for He-like singlet ($S = 0$) states. He-like singlet-state charge exchange spectra are similar to H-like spectra, with strong $n = 2 \to 1$ emission (line w) and significant high-n emission at low collision energies.


5.3. He-like spectra

He-like spectra resulting from the CX of H-like ions also have unique features that distinguish them from DE spectra. These spectra are somewhat more complicated than H-like spectra because the spins of the two electrons in He-like ions couple to yield either a singlet ($S = 0$) or triplet ($S = 1$) state. A 1:3 probability ratio is usually assumed based on the statistical weight of the levels, but statistical weights have been shown to be incorrect for some circumstances both experimentally and in detailed theoretical calculations [100, 131] for Be-like ions, which also have $S = 0$ and $S = 1$ states.

Figures 19 and 20 show schematic energy level diagrams for electron capture into $n = 4$ singlet and triplet states, respectively, assuming a uniform distribution of angular momentum states for illustrative purposes. The decay of the singlet states has essentially the same behavior as for H-like ions, yielding a prominent $n = 2 \to 1$ line (specifically the w "resonance" $1s2p\,^1P_1 \to 1s^2\,^1S_0$ transition, one of the four components of the $K\alpha$ complex; see below) along with some high-n K-series emission (especially at low collision energies, as is the case for H-like CX emission).

The triplet decay scheme is different, however, because the $\Delta S = 0$ selection rule forbids mixing, or "intercombination", of triplet and singlet states. As a result, *none* of the initial triplet states can decay directly to ground. Instead, all triplet states eventually decay to one of the $n = 2$ triplet states: $1s2s\,^3S_1$, or $1s2p\,^3P_2$, $^3P_1$, and $^3P_0$. From there they decay to ground via forbidden or semipermitted transitions.

Starting with the highest $n = 2$ energy level and proceeding to lower energies, the $^3P_2$ state is forbidden to decay to ground by the $\Delta J = 0, \pm 1$ (but no $J = 0 \to 0$) selection rule. It can decay via a $\Delta J = 2$ magnetic quadrupole (M2) transition
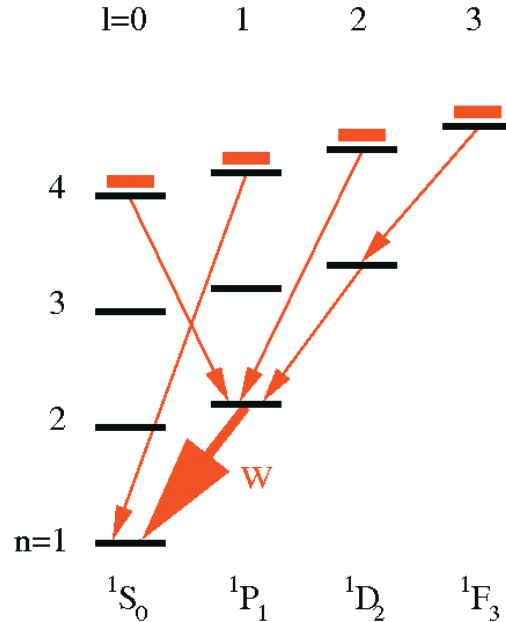
Fig. 20. Energy level diagrams for He-like triplet ($S = 1$) states (and the singlet $^1S_0$ ground state). High-n states cannot decay to ground because of the $\Delta S = 0$ selection rule, and instead decay to $n = 2$ states from which they decay via forbidden or semipermitted transitions (the z, y, and x lines), yielding $K\alpha$ emission.
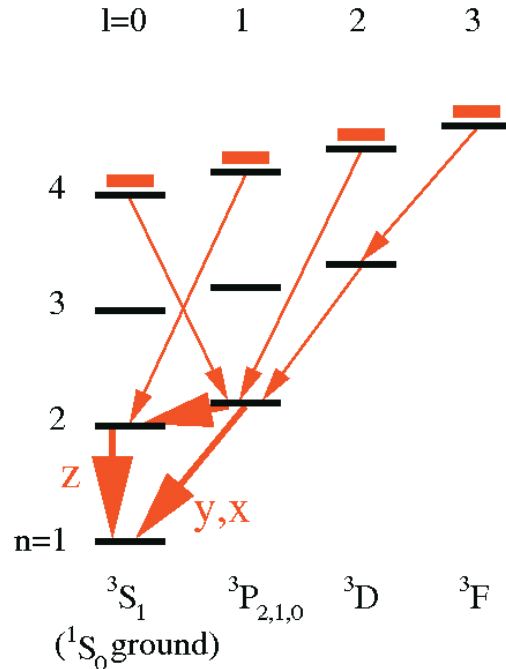
(yielding the x line, an "intercombination" transition so-called because it involves a change in S) but usually decays to the $^3S_1$ state. The $^3P_1$ state mixes slightly with the $^1P_1$ state in J–J

Fig. 21. H-like and He-like spectra from charge exchange of Fe ions with N_2 (adapted from ref. 84). High-n emission is more strongly enhanced in the H-like spectrum than in the He-like.

Fig. 22. H-like and He-like spectra from charge exchange of Xe ions with neutral Xe (adapted from ref. 125).
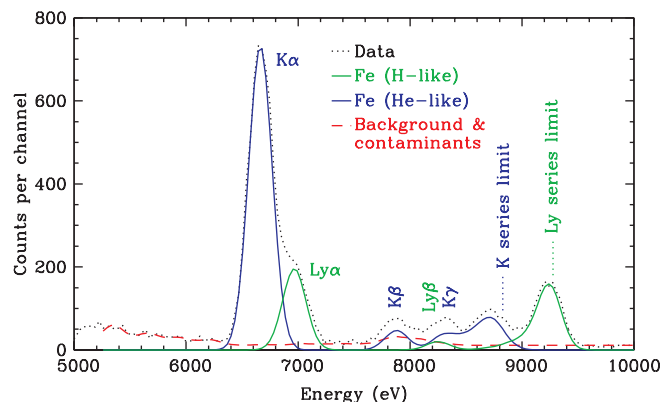

coupling and can therefore decay to ground via another intercombination transition to produce the y line. The $^3P_0$ state is strictly forbidden to decay by single-photon emission[5] because of the no $J = 0 \rightarrow 0$ rule and instead feeds the $^3S_1$ state, which is the lowest lying of all the triplet states. This metastable state eventually decays to ground via relativistic magnetic dipole (M1) decay, yielding the "forbidden" z line.

Most of the initial triplet states, therefore, end up yielding the z forbidden line or else the y intercombination line. Together with the weaker x line and the w resonance line, these make up the Kα complex, often but imprecisely referred to as the He-like triplet (after w, the often blended x and y, and z, and not to be confused with triplet, i.e., $S = 1$, states). Because triplet-state emission is usually several times as strong as singlet emission and the triplet emission is completely dominated by Kα, He-like CX spectra have weaker high-n emission than H-like spectra, although still stronger than in DE spectra. He-like and H-like CX spectra of Fe and Xe are shown in Figs. 21 and 22; He-like CX spectra have also been obtained on EBIT for U^{91+} + Ne [133], Au^{78+} + Ne [127], Kr^{35+} + Kr [134], Ar^{17+} + Ar [127], and Ne^{9+} + Ne [127, 130] (the latter with the XRS).

Although there is relatively little enhancement of He-like high-n lines, there are still large differences between DE and CX spectra. The much higher fraction of triplet states populated by CX than by DE leads to large differences in the relative intensities of the triplet and singlet lines, as shown in Fig. 23. Even if the z, y, x, and w lines can not be resolved from each other, the centroid energy of the Kα complex can often be determined precisely enough to distinguish between a CX or DE origin. As an example, based on the ~20 eV difference in the centroid energy of the He-like Fe Kα complex [84], Fujimoto et al. [54] concluded from a Suzaku observation of diffuse emission in the Galactic Center that cosmic-ray CX was not a significant contributor to the observed signal (see Sect. 3.3).
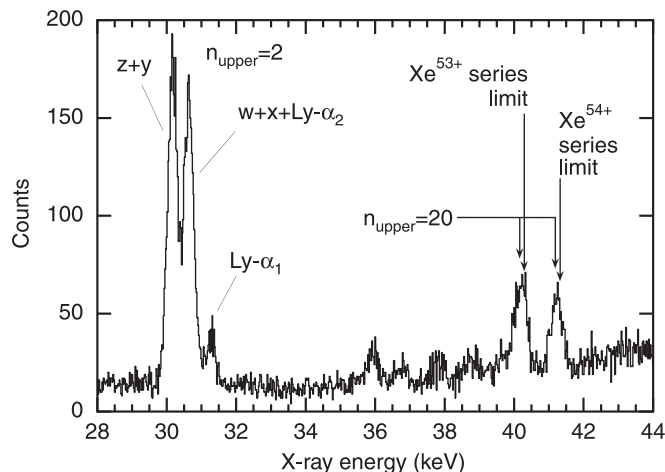
Fig. 23. Experimental He-like and H-like Fe spectra from direct excitation at 15 keV (top) and from charge exchange with N_2 (bottom). Both spectra were collected using the X-ray spectrometer microcalorimeter. The w line is relatively much weaker in the charge exchange spectrum and the Lyα_1/Lyα_2 ratio is nearly unity instead of 2:1.
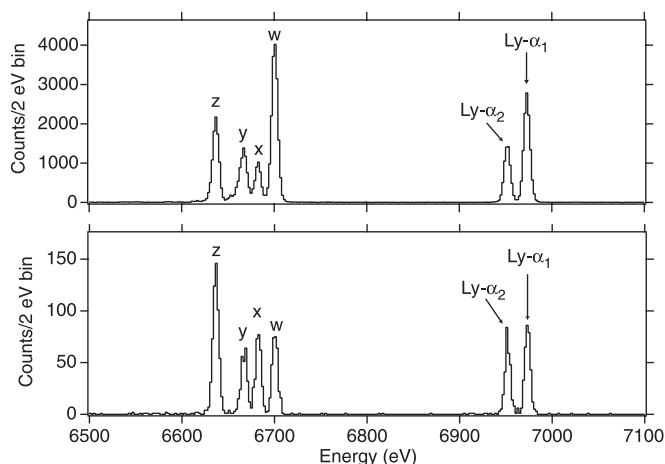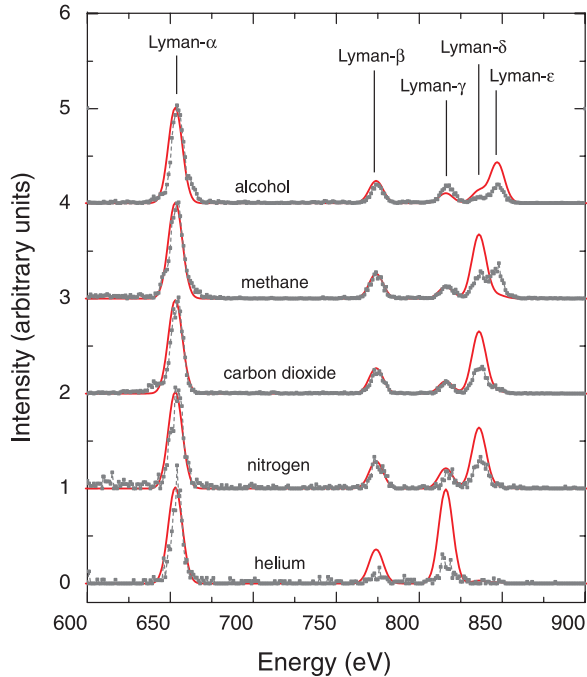

5.4. Multi-electron targets

Although the general features of CX spectra are largely independent of the target species, the effects of differing ionization potentials and multiple electrons can be quite pronounced, particularly on high-n emission lines. Figure 24 shows results from EBIT experiments and CTMC calculations for CX of bare O^{8+} with several targets of differing ionization potentials. As expected from its $\sqrt{I_H/I_n}$ dependence (see (1)), n_{max} decreases as the ionization potential increases. Similar behavior is seen in Fig. 25 for the high-n lines of H-like Fe for CX with N_2 (15.6 eV), H_2 (15.4 eV), and He (24.6 eV).

Theoretical models are less successful, however, in predicting line intensities. Model results using the classical trajectory Monte Carlo method are shown in Fig. 24. Although the model usually does a good job of predicting n_{max} for the O spectra, the intensities of high-n lines relative to Lyα, especially for n near n_{max} is often poor. For higher Z projectiles, discrepancies

---

[5]The only exception is in isotopes with a nonzero nuclear magnetic moment, which mixes $^3P_0$ with the $^3P_1$ state via the hyperfine interaction and thus enables decay to ground (for example, see ref. 132).

Fig. 24. Experimental and classical trajectory Monte Carlo model H-like O spectra from charge exchange of O^{8+} with several neutral gases. The n level of maximum likelihood for electron capture (n_{max}) decreases as the target ionization potential increases approximately as expected, but the observed high-n line intensities are generally smaller than predicted. Adapted from ref. 130.


Fig. 25. High-n Lyman lines from measurements of charge exchange of Fe^{26+} with various neutral gases illustrating the effect of target ionization potential. Although the qualitative behavior is as expected, observed values of n_{max} are larger than predicted by extrapolations from charge exchange with atomic H.

between theory and experiment also appear in n_{max}. In H-like Fe spectra (Fig. 25), the predicted n_{max} for CX with N_2 and H_2 is 12 or 13, while the observed value is 14 or 15. For He the expected value is 9 but the observed is 12.

The overall intensity of high-n emission with multi-electron targets can also be a surprise. Figure 26 plots the Lyman series hardness ratio ($\mathcal{H}$) for CX using several combinations of bare projectiles and targets. As can be seen, $\mathcal{H}$ is remarkably consistent. Theoretical calculations for CX with the many-electron target gases used in those experiments are not available, but CTMC model calculations for single-electron CX with H predict a steady decrease in $\mathcal{H}$ as Z increases. Multi-electron CX may be a significant process in these collisions, but the resulting autoionization of the multiply excited states following MEC will shift the resulting high-n Lyman emission to lower values of n, thus making it even more difficult to explain the higher than expected values of n_{max} that are observed in the Fe spectra. Whatever the contribution of MEC, it seems that the presence of multiple target electrons somehow increases the probability of capture into high-n p states that can decay directly to ground. The constancy of the hardness ratio across a wide range of H-like ions and many-electron targets suggests the existence of an underlying general process that perhaps could by approximated with relatively simple calculations.

Recent measurements at the Berlin EBIT [135] have confirmed the Livermore observation of the large hardness ratio observed for Ar^{17+} after interacting with neutral argon gas. The authors also extracted Ar^{18+} ions and, as in crossed-beam experiments, had them interact with an argon gas target. Sur-
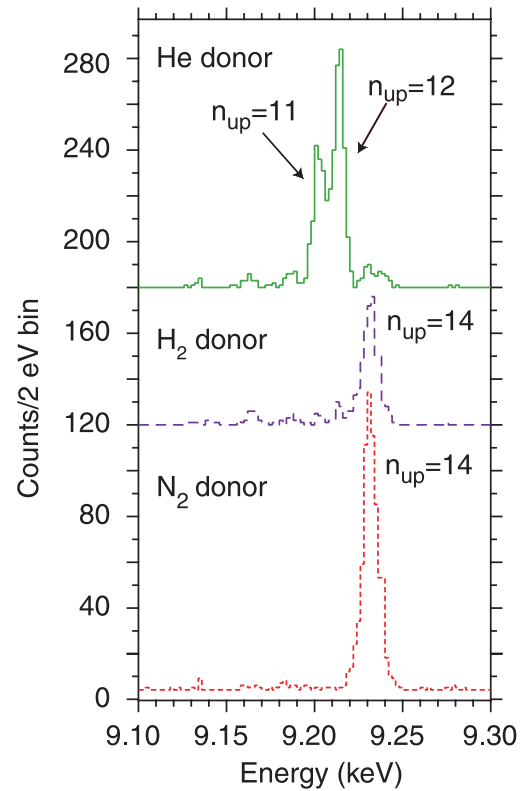
Fig. 26. Hardness ratios for H-like and He-like charge exchange emission as a function of Z, for collision energies of ~10 eV/amu. Broken lines through the H-like measurements (solid points) and He-like measurements (open circles) are drawn only to guide the eye. Neutral gases used in the experiments are CO_2 (for O) [36], Ne (for Ne) [128], Ar (for Ar) [127], N_2 (for Fe) [84], and Kr (for Kr) [127]. Results from classical trajectory Monte Carlo calculations ($\times$) for charge exchange with atomic H are extrapolated to Kr (continuous line). Adapted from ref. 84.
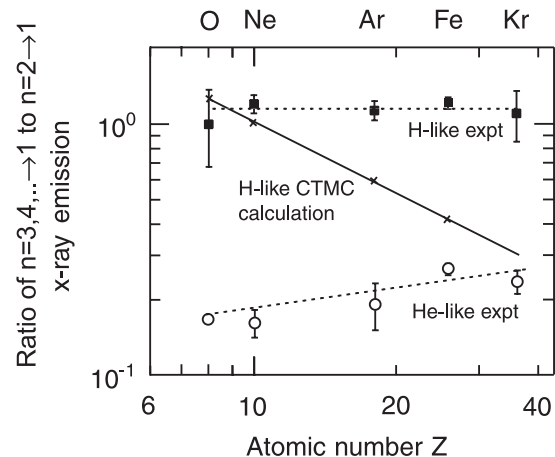
prisingly, the observed hardness ratio was much smaller and in line with the CTMC calculation shown in Fig. 25. This result suggests that conditions in the crossed-beam differ in some significant way from those in the EBIT measurement. One difference might be the effect of fields on level-specific CX cross sections, however, lowering the field strength (3 T during normal operation for both the Berlin and Livermore EBITs) did not change the observed high hardness ratio. Another possibility currently being investigated at Livermore is a change in ion temperature during the switch from electron trapping mode to the magnetic mode.

The difference in hardness ratios may also be caused by a large population in high-n metastable levels. Decay from those levels would not be observed in a crossed-beam experiment if the metastable ions exit the observation region before radiative decay can take place. A search for such levels using atomic structure calculations has not identified any possible candidate levels but those calculations were for singly excited states, i.e., they assumed single electron capture. The question, therefore, is still open whether there are metastable levels populated in multi-electron capture events that would lead to delayed X-ray emission from high-n levels.

6. Summary and future work

Electron beam ion traps, first demonstrated 20 years ago, have opened a new window on the study of charge exchange, just as CX has been recognized as an important mechanism in astrophysical X-ray emission. The development of X-ray microcalorimeters, which has proceeded roughly in parallel with that of EBITs, likewise promises rapid advances in the study of CX both in the laboratory and astrophysics.

As nondispersive spectrometers with much better energy resolution than Ge and Si(Li) solid-state detectors, microcalorimeters planned for use on rocket flights and future X-ray missions such as Constellation-X will permit detailed study of diffuse CX emission sources. At very low X-ray energies, specifically 100–284 eV (corresponding to the ROSAT 1/4 keV band), there have been glimpses of CX emission seen in Diffuse X-Ray Spectrometer (DXS; [136]) spectra, particularly the ~67.4 Å line, and by the X-Ray Quantum Calorimeter (XQC; [122]). The DXS was a moderate-resolution scanning-mode crystal spectrometer that flew on the Space Shuttle, and the XQC was a rocket-borne microcalorimeter. Strong solar-wind CX emission from L-shell ions such as Li-like Mg, Si, and S is expected in the 1/4 keV band (and at higher energies), in accord with the observation that the Long Term Enhancements seen by ROSAT were strongest in that band [48]. Currently there are no laboratory or theoretical data on such emission.

Another exciting opportunity for future research is the study of the relative population of $S = 1$ and $S = 0$ states in He-like ions formed by CX. As noted in Sect. 5.3, some work with Be-like ions (which, like He-like ions, have two valence electrons) indicates population ratios significantly different from the 3:1 expected from simple statistics, and recent theoretical work[6] suggests that CX of H-like ions with He at low energies leads

---

[6] P. Stancil. Private communication.

to initial population ratios much larger than 3:1. High-resolution EBIT spectra of He-like Kα emission such as shown in Fig. 23 will help resolve this question.

As discussed in Sect. 5.4, many questions posed by multi-electron CX remain to be addressed. Although EBITs cannot measure absolute CX cross sections, it should be possible to derive relative cross sections for SEC and DEC in some systems, as well as relative cross sections for CX of bare and H-like ions of the same element, which will supplement the limited data from low-energy crossed-beam experiments.

From an astrophysical perspective, H is the most important CX target. Atomic hydrogen is difficult to produce and work with in the laboratory, however, and very few CX measurements with H have been published, none with X-ray spectra at the several eV/amu energies used in EBITs. Experiments now underway with a new H source on the LLNL EBIT will hopefully provide important tests of theoretical models, particularly for higher q ions and low collision energies that can not be studied with other ion sources.

References

1. G.B. Field and G. Steigman. Astrophys. J. **166**, 59 (1971).
2. W.D. Watson. Rev. Mod. Phys. **48**, 513 (1976).
3. P.W. Blum and H.J. Fahr. Astron. Astrophys. **4**, 280 (1970).
4. R.K. Janev and H. Winter. Phys. Rep. **117**, 265 (1985).
5. H. Ryufuku and T. Watanabe. Phys. Rev. A, **20**, 1828 (1979).
6. K. Katsonis, G. Maynard, and R.K. Janev. Phys. Scr. **T37**, 80 (1991).
7. R. Abrines and I. Percival. Proc. Phys. Soc. **88**, 861 (1966).
8. R.E. Olson. Phys. Rev. A, **24**, 1726 (1981).
9. E.J. Smith, R.G. Marsden, A. Balogh, G. Gloeckler, J. Geiss, D.J. McComas, R.B. McKibben, R.J. MacDowall, L.J. Lanzerotti, N. Krupp, H. Krueger, and M. Landgraf. Science, **302**, 1165 (2003).
10. G.J. Fulks. J. Geophys. Res. **80**, 1701 (1975).
11. J.-Y. Chesnel, F. Frémont, B. Sulik, H. Merabet, C. Bedouet, X. Husson, M. Grether, and N. Stolterfoht. Nucl. Instrum. Methods: Phys. Res. B, **154**, 142 (1999).
12. V.A. Krasnopolsky, J.B. Greenwood, and P.C. Stancil. Space Sci. Rev. **113**, 271 (2004).
13. A. Dalgarno. Nucl. Instrum. Methods, **B9**, 655 (1985).
14. G.J. Ferland, K.T. Korista, and D.A. Verner. Astrophys. J. Lett. **481**, 115 (1997).
15. M. Arnaud and R. Rothenflug. Astron. Astrophys. Suppl. **60**, 425 (1985).
16. M. Arnaud and J. Raymond. Astrophys. J. **398**, 394 (1992).

17. P. Mazzotta, G. Mazzitelli, S. Colafrancesco, and N. Vittorio. Astron. Astrophys. Suppl. **133**, 403 (1998).

18. M.W. Wise and C.L. Sarazin. Astrophys. J. **345**, 384 (1989).

19. R. Lallement. Astron. Astrophys. **422**, 391 (2004).

20. A.P. Rasmussen, E. Behar, S.M. Kahn, J.W. den Herder, and K. van der Heyden. Astron. Astrophys. Lett. **365**, 231 (2001).

21. F.S. Porter, G.V. Brown, K.R. Boyce, R.L. Kelley, C.A. Kilbourne, P. Beiersdorfer, H. Chen, S. Terracol, S.M. Kahn, and A.E. Szymkowiak. Rev. Sci. Instrum. **75**, 3772 (2004).

22. C.M. Lisse, K. Dennerl, J. Englhauser, M. Harden, F.E. Marshall, M.J. Mumma, R. Petre, J.P. Pye, M.J. Ricketts, J. Schmitt, J. Trümper, and R.G. West. Science, **274**, 205 (1996).

23. T.E. Cravens. Geophys. Res. Lett. **24**, 105 (1997).

24. T.E. Cravens. Science, **296**, 1042 (2002).

25. C.M. Lisse, T.E. Cravens, and K. Dennerl. *In* Comets II, *Edited by* M.C. Festou, H.U. Keller, and H.A. Weaver. University of Arizona Press, Tucson. 2004. p. 631.

26. T.P. Sasseen, M. Hurwitz, C.M. Lisse, V. Kharchenko, D. Christian, S.J. Wolk, M.M. Sirk, and A. Dalgarno. Astrophys. J. **650**, 461 (2006).

27. V.A. Krasnopolsky. J. Geophys. Res. **111**, A12102 (2006).

28. A. Bhardwaj, R.F. Elsner, G.R. Gladstone, T.E. Cravens, C.M. Lisse, K. Dennerl, G. Branduardi-Raymont, B.J. Wargelin, J.H. Waite, Jr., I. Robertson, N. Østgaard, P. Beiersdorfer, S.L. Snowden, and V. Kharchenko. Planetary Space Sci. **55**, 1135 (2007).

29. R. von Steiger, N.A. Schwadron, L.A. Fisk, J. Geiss, G. Gloeckler, S. Hefti, B. Wilken, R.F. Wimmer-Schweingruber, and T.H. Zurbuchen. J. Geophys. Res. **105**, 27 217 (2000).

30. N.A. Schwadron and T.E. Cravens. Astrophys. J. **544**, 558 (2000).

31. V. Kharchenko and A. Dalgarno. J. Geophys. Res. **105**, 18351 (2000).

32. V.A. Krasnopolsky, D.J. Christian, V. Kharchenko, A. Dalgarno, S.J. Wolk, C.M. Lisse, and S.A. Stern. Icarus, **160**, 437 (2002).

33. M. Rigazio, V. Kharchenko, and A. Dalgarno. Phys. Rev. A, **66**, 64701 (2002).

34. R. Pepino, V. Kharchenko, A. Dalgarno, and R. Lallement. Astrophys. J. **617**, 1347 (2004).

35. B.J. Wargelin, M. Markevitch, M. Juda, V. Kharchenko, R. Edgar, and A. Dalgarno. Astrophys. J. **607**, 596 (2004).

36. P. Beiersdorfer, K.R. Boyce, G.V. Brown, H. Chen, S.M. Kahn, R.L. Kelley, M. May, R.E. Olson, F.S. Porter, C.K. Stahle, and W.A. Tillotson. Science, **300**, 1558 (2003).

37. K. Dennerl. Astron. Astrophys. **394**, 1119 (2002).

38. H. Gunell, M. Holmström, E. Kallio, P. Janhunen, and K. Dennerl. Geophys. Res. Lett. **31**, L22801 (2004).

39. K. Dennerl, C.M. Lisse, A. Bhardwaj, V. Burwitz, J. Englhauser, H. Gunell, M. Holmström, F. Jansen, V. Kharchenko, and P.M. Rodríguez-Pascual. Astron. Astrophys. **451**, 709 (2006).

40. G.R. Gladstone, J.H. Waite, D. Grodent, W.S. Lewis, F.J. Crary, R.F. Elsner, M.C. Weisskopf, T. Majeed, J.-M. Jahn, A. Bhardwaj, J.T. Clarke, D.T. Young, M.K. Dougherty, S.A. Espinosa, and T.E. Cravens. Nature, **415**, 1000 (2002).

41. R.F. Elsner, N. Lugaz, J.H. Waite, T.E. Cravens, G.R. Gladstone, P. Ford, D. Grodent, A. Bhardwaj, R.J. MacDowall, M.D. Desch, and T. Majeed. J. Geophys. Res. **110**, A01207 (2005).

42. G. Branduardi-Raymont, R.F. Elsner, G.R. Gladstone, G. Ramsay, P. Rodriguez, R. Soria, and J.H. Waite, Jr. Astron. Astrophys. **424**, 331 (2004).

43. G. Branduardi-Raymont, A. Bhardwaj, R.F. Elsner, G.R. Gladstone, G. Ramsay, P. Rodriguez, R. Soria, J.H. Waite, Jr., and T.E. Cravens. Astron. Astrophys. **463**, 761 (2007).

44. T.E. Cravens, J.H. Waite, T.I. Gombosi, N. Lugaz, G.R. Gladstone, B.H. Mauk, and R.J. MacDowall. J. Geophys. Res. **108**, 1465.

45. E.J. Bunce, S.W.H. Cowley, and T.K. Yeoman. J. Geophys. Res. **109**, A09S13.

46. V. Kharchenko, A. Dalgarno, D.R. Schultz, and P.C. Stancil. Geophys. Res. Lett. **33**, L11105.

47. K. Dennerl, V. Burwitz, J. Englhauser, C. Lisse, and S. Wolk. Astron. Astrophys. **386**, 319 (2002).

48. S.L. Snowden, M.J. Freyberg, P.P. Plucinsky, J.H.M.M. Schmitt, J. Trümper, W. Voges, R.J. Edgar, D. McCammon, and W.T. Sanders. Astrophys. J. **454**, 643 (1995).

49. M.J. Freyberg. *In* The local bubble and beyond. *Edited by* D. Breitschwerdt, M.J. Freyberg, and J. Trümper. Springer, Berlin. 1998. p. 113.

50. T.E. Cravens, I.P. Robertson, and S.L. Snowden. J. Geophys. Res. **106**, 24883 (2001).

51. R.K. Smith, R.J. Edgar, P.P. Plucinsky, B.J. Wargelin, P.E. Freeman, and B.A. Biller. Astrophys. J. **623**, 225 (2005).

52. R.C. Hickox and M. Markevitch. Astrophys. J. **645**, 95 (2006).

53. S.L. Snowden, M.R. Collier, and K.D. Kuntz. Astrophys. J. **610**, 1182 (2004).

54. R. Fujimoto, K. Mitsuda, D. McCammon, Y. Takei, M. Bauer, Y. Ishisaki, F.S. Porter, H. Yamaguchi, K. Hayashida, and N.Y. Yamasaki. Publ. Astron. Soc. Jpn. **59**, 133 (2007).

55. D.B. Henley and R.L. Shelton. astro-ph 0703189 (2007).

56. I.P. Robertson and T.E. Cravens. J. Geophys. Res. **108**, 8031 (2003).

57. I.P. Robertson and T.E. Cravens. Geophys. Res. Lett. **30**, 1439 (2003).

58. I.P. Robertson, M.R. Collier, T.E. Cravens, and M.-C. Fok. J. Geophys. Res. **111**, A12105 (2006).

59. D.P. Cox. *In* The local bubble and beyond. *Edited by* D. Breitschwerdt, M.J. Freyberg, and J. Trümper. Springer, Berlin. 1998. p. 121.

60. T.E. Cravens. Astrophys. J. Lett. **532**, L153 (2000).

61. R. Lallement. Astron. Astrophys. **418**, 143 (2004).

62. D. Koutroumpa, R. Lallement, V. Kharchenko, A. Dalgarno, R. Pepino, V. Izmodenov, and E. Quémerais. Astron. Astrophys. **460**, 289 (2006).

63. B.J. Wargelin and J.J. Drake. Astrophys. J. Lett. **546**, L57 (2001).

64. B.J. Wargelin and J.J. Drake. Astrophys. J. **578**, 503 (2002).

65. R.K. Smith, M.W. Bautz, R.J. Edgar, R. Fujimoto, K. Hamaguchi, J.P. Hughes, M. Ishida, R. Kelley, C.A. Kilbourne, K.D. Kuntz et al. Publ. Astron. Soc. Jpn. **59**, 141 (2007).

66. M. Hurwitz, T.P. Sasseen, and M.M. Sirk. Astrophys. J. **623**, 911 (2005).

67. J.N. Bregman and E.J. Lloyd-Davies. Astrophys. J. **644**, 167 (2006).

68. J. Nevalainen, M. Bonamente, and J. Kaastra. Astrophys. J. **656**, 733 (2007).

69. D.M. Worrall, F.E. Marshall, E.A. Boldt, and J.H. Swank. Astrophys. J. **255**, 111 (1982).

70. K. Koyama, Y. Maeda, T. Sonobe, T. Takeshima, Y. Tanaka, and S. Yamauchi. Publ. Astron. Soc. Jpn. **48**, 249 (1996).

71. H. Kaneda, K. Makishima, S. Yamauchi, K. Koyama, K. Matsuzaki, and N.Y. Yamasaki. Astrophys. J. **491**, 638 (1997).

72. K. Ebisawa, Y. Maeda, H. Kaneda, and S. Yamauchi. Science, **293**, 1633 (2001).

73. M.P. Muno, F.K. Baganoff, M.W. Bautz, E.D. Feigelson, G.P. Garmire, M.R. Morris, S. Park, G.R. Ricker, and L.K. Townsley. Astrophys. J. **613**, 326 (2004).

74. M. Revnivtsev, S. Sazonov, M. Gilfanov, E. Churazov, and R. Sunyaev. Astron. Astrophys. **452**, 169 (2006).

75. Y. Tanaka, T. Miyaji, and G. Hasinger. Astron. Nachr. **320**, 181 (1999).

76. Y. Tanaka. Astron. Astrophys. **382**, 1052 (2002).

77. J. Silk and G. Steigman. Phys. Rev. Lett. **23**, 597 (1969).

78. W.D. Watson. Astrophys. J. **206**, 842 (1976).

79. R.W. Bussard, R. Ramaty, and K. Omidvar. Astrophys. J. **220**, 353 (1978).

80. D.W. Rule and K. Omidvar. Astrophys. J. **229**, 1198 (1979).

81. D.K. Strickland and T.M. Heckman. Astrophys. J. **658**, 258 (2007).

82. P.P. Kronberg, S.A. Colgate, H. Li, and Q.W. Dufton. Astrophys. J. Lett. **604**, L77 (2004).

83. K. Koyama, H. Yoshiaki, T. Inui, H. Nakajima, H. Matsumoto, T.G. Tsuru, T. Takahashi, Y. Maeda, N.Y. Yamazaki al. Publ. Astron. Soc. Jpn. **59**, 245 (2007).

84. B.J. Wargelin, P. Beiersdorfer, P.A. Neill, R.E. Olson, and J.H. Scofield. Astrophys. J. **634**, 687 (2005).

85. E. Churazov, R. Sunyaev, S. Sazonov, and M. Revnivtsev. Mon. Not. R. Astron. Soc. **357**, 1377 (2005).

86. P. Jean, J. Knödlseder, W. Gillard, N. Guessoum, K. Ferrière, A. Marcowith, V. Lonjou, and J.P. Roques. Astron. Astrophys. **445**, 579 (2006).

87. X. Ma, T. Stöhlker, F. Bosch, O. Brinzanescu, S. Fritzsche, C. Kozhuharov, T. Ludziejewski, P.H. Mokler, Z. Stachura, and A. Warczak. Phys. Rev. A, **64**, 012704 (2001).

88. J.B. Greenwood, I.D. Williams, S.J. Smith, and A. Chutjian. Astrophys. J. Lett. **533**, L175 (2000).

89. J.B. Greenwood, I.D. Williams, S.J. Smith, and A. Chutjian. Phys. Rev. A, **63**, 062707 (2001).

90. R. Ali, P.A. Neill, P. Beiersdorfer, C.L. Harris, M.J. Raković, J.G. Wang, D.R. Schultz, and P.C. Stancil. Astrophys. J. Lett. **629**, L125 (2005).

91. R. Ali, C.L. Locke, M.L.A. Raphaelian, and M. Stockli. Phys. Rev. A, **49**, 3586 (1994).

92. A.A. Hasan, F. Eissa, and R. Ali. Astrophys. J. Lett. **560**, L201 (2001).

93. X. Fléchard, C. Harel, H. Jouin, B. Pons, L. Adoui, F. Frémont, A. Cassimi, and D. Hennecart. J. Phys. B, **34**, 2759 (2001).

94. D. Fischer, B. Feuerstein, R.D. DuBois, R. Moshammer, J.R. Crespo López-Urrutia, I. Draganic, H. Lörch, A.N. Perumal, and J. Ullrich. J. Phys. B, **35**, 1369 (2002).

95. E. Edgu-Fry, A. Wech, J. Stuhlman, T.G. Lee, C.D. Lin, and C.L. Cocke. Phys. Rev. A, **69**, 052714 (2004).

96. D. Bodewits, A.G.G.M. Tielens, R. Morgenstern, and R. Hoekstra. Nucl. Instrum. Methods Phys. Res. B, **235**, 358 (2005).

97. B. Seredyuk, R.W. McCullough, H. Tawara, H.B. Gilbody, D. Bodewits, R. Hoekstra, A.G.G.M. Tielens, P. Sobocinski, D. Pesic, R. Hellhammer, B. Sulik, N. Stolterfoht, O. Abu-Haija, and E.Y. Kamber. Phys. Rev. A, **71**, 022705 (2005).

98. G. Lubinski, Z. Juhász, R. Morgenstern, and R. Hoekstra. Phys. Rev. Lett. **86**, 616 (2001).

99. D. Bodewits, Z. Juhász, R. Hoekstra, and A.G.G.M. Tielens. Astrophys. J. Lett. **606**, L81 (2004).

100. F.W. Bliek, G.R. Woestenenk, R. Morgenstern, and R. Hoekstra. Phys. Rev. A, **57**, 221 (1998).

101. G. Lubinski, Z. Juhász, R. Morgenstern, and R. Hoekstra. J. Phys. B, **33**, 5275 (2000).

102. T. Ehrenreich, K. Miller, P. Gee, Q. Kessel, E. Pollack, W.W. Smith, N. Djuric, J. Lozano, S.J. Smith, and A. Chutjian. *In* X-ray diagnostics of astrophysical plasmas: theory, experiment, and observation, CP774. *Edited by* R. Smith. AIP, Melville, New York. 2005. p. 281.

103. P. Beiersdorfer, M. Bitter, M. Marion, and R.E. Olson. Phys. Rev. A, **72**, 032725 (2005).

104. E. Källne, J. Källne, A. Dalgarno, J.E.R.E.S. Marmar, and A.K. Pradhan. Phys. Rev. Lett. **52**, 2245 (1984).

105. J.E. Rice, E.S. Marmar, J.L. Terry, E. Källne, and J. Källne. Phys. Rev. Lett. **56**, 50 (1986).

106. R.E. Marrs. Can. J. Phys. **86** (2008). This issue.

107. M.A. Levine, R.E. Marrs, J.R. Henderson, D.A. Knapp, and M.B. Schneider. Phys. Scr. **T22**, 157 (1988).

108. M.A. Levine, R.E. Marrs, J.N. Bardsley, P. Beiersdorfer, C.L. Bennett, M.H. Chen, T. Cowan, D. Dietrich, J.R. Henderson, D.A. Knapp et al. Nucl. Instrum. Methods B, **43**, 431 (1989).

109. B.M. Penetrante, M.A. Levine, and J.N. Bardsley. *In* International Symposium on Electron Beam Ion Sources and Their Applications, *Edited by*. A. Hershcovitch. AIP Conf. Proc. No. 188. AIP, New York. 1989. p. 145.

110. M.B. Schneider, M.A. Levine, C.L. Bennet, J.R. Henderson, D.A. Knapp, and R.E. Marrs. *In* International Symposium on Electron Beam Ion Sources and Their Applications, *Edited by* A. Hershcovitch. AIP Conf. Proc. No. 188. AIP, New York. 1989. p. 158.

111. B.M. Penetrante, J.N. Bardsley, M.A. Levine, D.A. Knapp, and R.E. Marrs. Phys. Rev. A, **43**, 4873 (1991).

112. P. Beiersdorfer, V. Decaux, S.R. Elliott, K. Widmann, and K. Wong. Rev. Sci. Instrum. **66**, 303 (1995).

113. P. Beiersdorfer, V. Decaux, and K. Widmann. Nucl. Instrum. Methods B, **98**, 566 (1995).

114. P. Beiersdorfer, A.L. Osterheld, V. Decaux, and K. Widmann. Phys. Rev. Lett. **77**, 5353 (1996).

115. P. Beiersdorfer, J. Crespo López-Urrutia, E. Förster, J. Mahiri, and K. Widmann. Rev. Sci. Instrum. **68**, 1077 (1997).

116. P. Beiersdorfer, L. Schweikhard, J. Crespo López-Urrutia, and K. Widmann. Rev. Sci. Instrum. **67**, 3818 (1996).

117. L. Schweikhard, P. Beiersdorfer, and E. Träbert. AIP Conf. Proc. **606**, 174 (2002).

118. P. Beiersdorfer, B. Beck, R.E. Marrs, S.R. Elliott, and L. Schweikhard. Rapid Commun. Mass Spectrom. **8**, 141 (1994).

119. P. Beiersdorfer, St. Becker, B. Beck, S. Elliott, K. Widmann, and L. Schweikhard. Nucl. Instrum. Methods Phys. Res. B, **98**, 558 (1995).

120. P. Beiersdorfer, R.E. Olson, G.V. Brown, C.L. Harris, P.A. Neill, L. Schweikhard, S.B. Utter, and K. Widmann. Phys. Rev. Lett. **85**, 5090 (2000).
121. E. Silver, S. Bandler, H. Schnopper, S. Murray, N. Madden, D. Landis, F. Goulding, J. Beeman, E.E. Haller, and M. Barbera. AIP Conf. Proc. **605**, 555 (2002).
122. D. McCammon, R. Almy, E. Apodaca, W. Bergmann Tiest, W. Cui, S. Deiker, M. Galeazzi, M. Juda, A. Lesser, T. Mihara, J.P. Morgenthaler, W.T. Sanders, J. Zhang, et al. Astrophy. J. **576**, 188 (2002).
123. R.L. Kelley. Publ. Astron. Soc. Jpn. **59**, 77 (2007).
124. F.S. Porter, B.R. Beck, P. Beiersdorfer, K.R. Boyce, G.V. Brown, H. Chen, J. Gygax, S.M. Kahn, R.L. Kelley, C.A. Kilbourne, E. Magee, and D.B. Thorn. Can. J. Phys. **86** (2008). This issue.
125. J.A. Perez, R.E. Olson, and P. Beiersdorfer. J. Phys. B, **34**, 3063 (2001).
126. G.V. Brown, et al. Nucl. Instrum. Methods Phys. Res. A, **559**, 623 (2006).
127. P. Beiersdorfer, R.E. Olson, G.V. Brown, H. Chen, C.L. Harris, P.A. Neill, L. Schweikhard, S.B. Utter, and K. Widmann. Phys. Rev. Lett. **85**, 5090 (2000).
128. P. Beiersdorfer, C.M. Lisse, R.E. Olson, G.V. Brown, and H. Chen. Astrophys. J. Lett. **549**, L147.
129. P. Beiersdorfer, H. Chen, K.R. Boyce, G.V. Brown, R.L. Kelley, C.A. Kilbourne, F.S. Porter, and S.M. Kahn. Nucl. Instrum. Methods Phys. Res. B, **235**, 116 (2005).
130. S. Otranto, R.E. Olson, and P. Beiersdorfer. Phys. Rev. A, **73**, 022723 (2006).
131. P.C. Stancil, B. Zygelman, N.J. Clarke, and D.L. Cooper. J. Phys. B, **30**, 1013 (1997).
132. K.L. Wong, P. Beiersdorfer, K.J. Reed, and D.A. Vogel. Phys. Rev. A, **51**, 1214 (1995).
133. L. Schweikhard, P. Beiersdorfer, G.V. Brown, J.R. Crespo López-Urrutia, S.B. Utter, and K. Widmann. Nucl. Instrum. Methods Phys. Res. B, **142**, 245 (1998).
134. P. Beiersdorfer, L. Schweikhard, R. Olson, G.V. Brown, S.B. Utter, J.R. Crespo López-Urrutia, and K. Widmann. Phys. Scr. **T80**, 121 (1999).
135. F.I. Allen, C. Biedermann, R. Radtke, and G. Fussmann. J. Phys. Conf. Ser. **58**, 188 (2007).
136. W.T. Sanders, R.J. Edgar, W.L. Kraushaar, D. McCammon, and J.P. Morgenthaler. Astrophys. J. **554**, 694 (2001).